Article

Age-dependent regulation of axoglial interactions and behavior by oligodendrocyte AnkyrinG

Xiaoyun Ding [1], Yu Wu [1], Anna Vainshtein[2], Victoria Rodriguez[3], Emily Ricco[3], James T. Okoh[1], Yanhong Liu [1], Daniel C. Kraushaar[3], Elior Peles [2] & Matthew N. Rasband [1] ✉

The bipolar disorder (BD) risk gene *ANK3* encodes the scaffolding protein AnkyrinG (AnkG). In neurons, AnkG regulates polarity and ion channel clustering at axon initial segments and nodes of Ranvier. Disruption of neuronal AnkG causes BD-like phenotypes in mice. During development, AnkG is also expressed at comparable levels in oligodendrocytes and facilitates the efficient assembly of paranodal junctions. However, the physiological roles of glial AnkG in the mature nervous system, and its contributions to BD-like phenotypes, remain unexplored. Here, we show that oligodendroglia-specific AnkG conditional knockout results in destabilization of axoglial interactions in aged but not young adult mice. In addition, these mice exhibit significant histological, electrophysiological, and behavioral pathophysiologies. Unbiased translatomic profiling reveals potential compensatory machineries. These results highlight the functions of glial AnkG in maintaining proper axoglial interactions throughout aging and suggest a contribution of glial AnkG to neuropsychiatric disorders.

The cytoskeletal scaffolding protein AnkyrinG (AnkG) is a master regulator of ion channel clustering and neuronal polarity[1,2]. In neurons, the ankyrin-repeat domain of AnkG clusters ion channels, transporters, receptors, and cell adhesion molecules to distinct membrane domains of the axon, while the spectrin-binding domain anchors them to the underlying periodic spectrin-actin cytoskeleton[3]. Thus, AnkG dictates the formation of the axon initial segments (AIS) and nodes of Ranvier, where action potentials are initiated and efficiently propagated via saltatory conduction[4,5]. The nodes of Ranvier are flanked by the paranodal junctions (PNJs) which are specialized axoglial junctions between myelinating oligodendrocytes and the axon. PNJs are essential for the formation and maintenance of the nodes of Ranvier and proper action potential conduction[6,7]. As membrane diffusion barriers, PNJs and their associated cytoskeleton restrict sodium channels to the nodes and voltage-gated potassium channels (Kv1) to the juxtaparanodes[8,9].

PNJs consist of the axonal cell adhesion molecules (CAMs) Contactin and Contactin-Associated Protein (Caspr), and the 155 kDa glial form of the CAM Neurofascin (NF155)[10–12]. The axonal CAMs recruit βII spectrin and protein 4.1b to create a cytoskeletal barrier that restricts ion channels and other membrane proteins to nodes and juxtaparanodes[8,13,14]. In glia, NF155 is secured to the underlying cytoskeleton network by ankyrin scaffolding proteins—AnkG in the central nervous system (CNS) and AnkyrinB (AnkB) in the peripheral nervous system (PNS). During early CNS development, glial AnkG facilitates the rapid and efficient assembly of paranodal junctions[15]. However, the role of glial AnkG beyond early development remains unclear.

The AnkG coding gene, *ANK3*, is a risk gene for many neuropsychiatric disorders, including autism spectrum disorder (ASD), schizophrenia (SCZ), and bipolar disorder (BD)[16–18]. Several genetic variants of *ANK3* have been identified by GWAS and a few validated using *Drosophila* or mouse models[19]. For instance, *Ank3* heterozygous

[1]Department of Neuroscience, Baylor College of Medicine, Houston, TX 77030, USA. [2]Department of Molecular Cell Biology, Weizmann Institute of Science, Rehovot 76100, Israel. [3]Genomic and RNA Profiling Core, Baylor College of Medicine, Houston, TX 77030, USA. ✉e-mail: rasband@bcm.edu

1

knockout mice demonstrate various behavioral abnormalities mimicking BD in humans[20], including decreased anxiety and increased motivation for reward. Other studies examined the underlying mechanism of BD-like phenotypes and contributions from different subtypes of neurons. For example, deletion of *Ank3* from either forebrain pyramidal neurons or PV interneurons[21,22] could each lead to robust phenotypes. These observations suggest that the underlying functions of *ANK3* and its association with BD risk may be multifaceted with contributions from many different cell types. In particular, despite a comparable level of *Ank3* transcripts in both neurons and oligodendrocytes[23], the functions of glial AnkG remain poorly understood, especially in adults.

Here, we show that oligodendrocyte specific *Ank3* knockout mice display destabilization of PNJs during aging, which is accompanied by histological, electrophysiological, behavioral, and translatomic alterations. Our results reveal functions of oligodendroglial AnkG in the maintenance of the PNJ and suggest potential contributions of glial AnkG to psychiatric disease.

Results

Loss of oligodendroglial AnkG exacerbates age-related paranode disruption

Glial AnkG facilitates the rapid and efficient assembly of PNJs during early development[15]. However, whether glial AnkG is functionally required beyond the perinatal stage remains unknown. Therefore, we generated oligodendroglial specific conditional knock-out mice by crossing *Ank3^{F/F}* with *NG2^{Cre}* mice (AnkG cKO). Upon Cre-mediated recombination, exons 23 and 24 of *Ank3* are excised, resulting in premature stop codons in exons 25 and 26 (Fig. 1a). To confirm the efficient loss of AnkG protein in cKO animals, we performed immunoblotting of whole brain homogenates from 2 month-old mice (Fig. 1b). We observed a significant reduction of the glial isoforms of AnkG (270 kDa and 190 kDa)[15] from cKO mice compared to littermate controls (Fig. 1b, c). To further evaluate the cell-type specificity of AnkG loss in AnkG cKO mice, we performed immunofluorescence staining of the optic nerve in 2 month-old mice. We found consistent loss of paranodal (glial) AnkG (Fig. 1d, **arrowheads**), while nodal (neuronal) AnkG (colocalizing with βIV spectrin) remained unaffected.

To determine if the PNJ structure is disrupted in young AnkG cKO mice, we performed immunofluorescence labeling for Neurofascin (nodes and paranodes), Caspr (paranodes), and Kv1.2 (juxtaparanodes). Consistent with our previous results using *CNP^{Cre}; Ank3^{F/F}* mice[15], the PNJ structure was intact at 2 months-of-age in AnkG cKO mice. This suggests that early developmental deletion of AnkG from oligodendrocytes may be effectively compensated for by redundant mechanisms in young adults.

Like AnkG cKO mice, we previously reported that loss of βII spectrin from Schwann cells also delays the assembly of PNJs during development[24]. Intriguingly, adult βII spectrin cKO mice were phenotypically normal until 60 weeks of age, when they began to show disrupted paranodes in the PNS and CNS. Since AnkG and βII spectrin can interact—likely in a complex at the PNJ—we reasoned that loss of paranodal AnkG might also cause age-dependent deterioration of the PNJ. Therefore, we performed histological analyses of the paranodal structure in 14 month-old AnkG cKO animals (Fig. 1e) with sex-matched littermate controls. Interestingly, we observed no significant changes in paranodal organization of small-diameter axons in the AnkG cKO optic nerve. However, there was clear disruption and "unwinding" of paranodal Caspr in large-diameter axons in the spinal cord of 14 month-old AnkG cKO mice. These disruptions are shown by line scan analysis of nodal NF186, paranodal Caspr, and juxtaparanodal Kv1.2 (Fig. 1f, g). We found a 2.8-fold increase in the frequency of disrupted paranodes in the large-diameter axons of 14 month-old AnkG cKO mice compared to control mice (Fig. 1h). However, the frequency of disrupted paranodes in small diameter axons was comparable between

AnkG cKO and control mice (Fig. 1h). These data suggest that oligodendroglial AnkG is required to maintain the PNJ in large-diameter axons in older adult mice.

Loss of oligodendroglial AnkG results in more frequent nodes of Ranvier

To determine whether the molecular composition of the PNJs is altered in AnkG cKO mice, we extracted proteins from spinal cord homogenates of AnkG cKO and control mice at 14 months of age. Using immunoblotting, we examined the protein level of PNJ components Caspr, Contactin, and Neurofascin (both nodal NF186 and paranodal NF155) (Fig. 2a). While Caspr expression remained comparable in AnkG cKO mice compared to control mice (Fig. 2b), there was a significant decrease in Contactin expression (Fig. 2c). Interestingly, we observed a ~1.4-fold increase in the amount of NF186 in AnkG cKO mice compared to control mice, whereas NF155 remained comparable (Fig. 2e). This difference is further illustrated by a ~30% decrease in the ratio between NF155 and NF186 (Fig. 2f). One possible explanation for these results is the presence of more nodes of Ranvier in the AnkG cKO mice. Therefore, we performed nearest neighbor analysis on the nodes of Ranvier in 14 month-old optic nerve sections, using βIV spectrin as a marker for nodes of Ranvier. We observed a significant decrease in the average nearest node distance (Fig. 2g). This is further illustrated by the frequency distribution of nearest node distance in AnkG cKO mice compared to control mice (Fig. 2h).
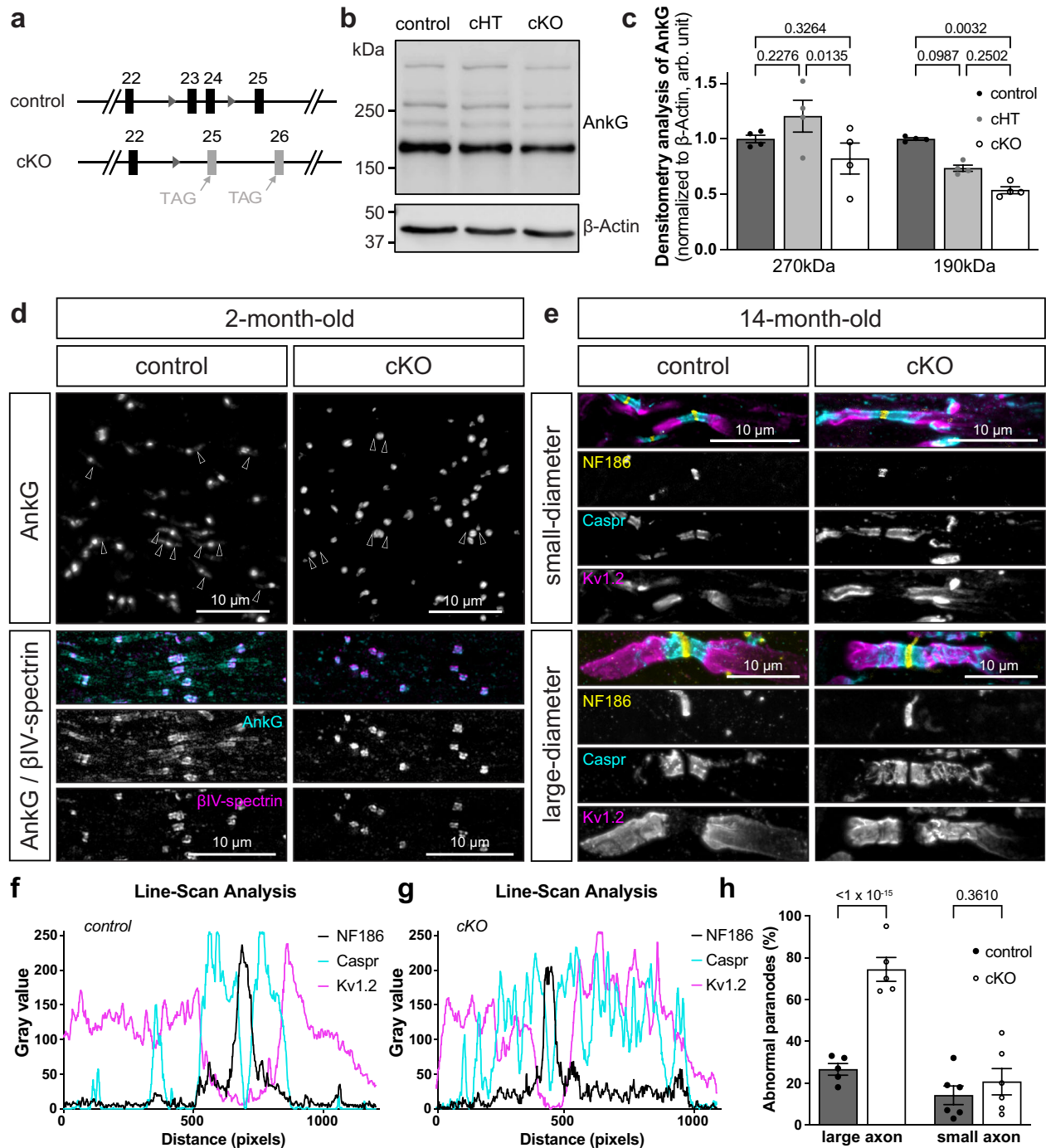
Loss of oligodendroglial AnkG results in thinner myelin sheaths

What could account for more nodes of Ranvier? Reduced internodal lengths in AnkG cKO mice could explain the increased number of nodes, and shorter internodal lengths are accompanied by thinner myelin. To determine if AnkG cKO mice have thinner myelin, we performed transmission electron microscopy analysis on the optic nerves of 16 month-old littermate control, AnkG cHT, and AnkG cKO mice (Fig. 3a). Although we did not observe significant alterations in the overall compactness of the myelin sheaths among genotypes, we found a small, but significant increase in g-ratio in AnkG cKO mice compared to that of control mice (Fig. 3b, c), indicating that AnkG cKO mice have thinner myelin.

The defects in the myelin sheath could reflect an overall reduction in the number of mature OLs in the absence of AnkG, either due to proliferation, differentiation, or survival of OL lineage cells. To test this possibility, we quantified the density of CC1+ cells in 14 month-old AnkG cKO and control mice (Fig. 3d). However, we found no significant difference between the AnkG cKO and control mice (Fig. 3e). We then examined whether the total amount of myelin is changed using Myelin Basic Protein (MBP) as a marker by both immunofluorescence staining and immunoblotting in 14 month-old mice (Fig. 3d, g). We found a significant reduction in the fluorescence intensity of MBP in the optic nerve of 14 month-old AnkG cKO mice compared to control mice (Fig. 3d, f). Similarly, immunoblot analysis confirmed a significant reduction in the total amount of MBP in the spinal cord of 14 month-old AnkG cKO mice compared to control (Fig. 3g, h). Together, these results show that loss of oligodendroglial AnkG results in less myelin but does not affect oligodendrocyte differentiation.

AnkG cKO mice have slower action potential conduction

Proper myelination and axoglial interactions ensure efficient propagation of action potentials (APs). Given the disrupted paranodal structure, shorter internodal length and thinner myelin in the optic nerve, we reasoned that the conduction velocity of action potentials in the CNS might be affected in aged AnkG cKO mice. To evaluate AP conduction, we measured compound action potentials (CAPs) from the optic nerves of 12–16 month-old control and AnkG cKO mice using suction electrodes[25]. CAPs were fitted with three gaussian curves corresponding to the three major groups of axons—slow, medium, and

Fig. 1 | Loss of oligodendroglial AnkG leads to destabilization of paranodal junctions during aging. a Schematic of the *Ank3* conditional allele and *NG2^Cre^*-mediated recombination. **b** Immunoblot for AnkG in whole brain homogenates from 2 month-old control (*Ank3^F/F^*), AnkG cHT (*NG2^Cre+^;Ank3^F/+^*), and AnkG cKO (*NG2^Cre+^;Ank3^F/F^*) animals. All three major isoforms of AnkG (480 kDa, 270 kDa, 190 kDa) are detected. β-Actin is the loading control. **c** Densitometry analysis of AnkG (270 and 190 kDa isoforms) in the brains of 2 month-old control, cHT, and cKO mice. N = 4 for each genotype. Two-way ANOVA with multiple comparisons. 270 kDa WT vs cHT: $t = 2.423$, DF = 18.00; WT vs cKO: $t = 2.084$, DF = 18.00; cHT vs cKO: $t = 4.507$, DF = 18.00. 190 kDa WT vs cHT: $t = 3.108$, DF = 18.00; WT vs cKO: $t = 5.445$, DF = 18.00; cHT vs cKO: $t = 2.337$, DF = 18.00. **d** Representative immuno-fluorescence staining of AnkG and βIV spectrin in the optic nerve of 2 month-old control and cKO mice. Arrowheads indicate paranodes. Scale bar, 10 μm. (Cyan:

AnkG, Magenta: βIV-spectrin) from at least 3 independent experiments.
e Immunofluorescence labeling of nodal (Yellow: Neurofascin186), paranodal (Cyan: Caspr) and juxtaparanodal (Magenta: Kv1.2) proteins in the spinal cord of 14 month-old control and cKO mice. Severe paranodal unwinding is only observed in the large-diameter axons. From at least 3 independent experiments. Scale bar, 10 μm. **f**–**g** Line-scan analysis of nodes of Ranvier on large-diameter axons of control (**f**) and cKO (**g**) mice. Black: Neurofascin186, cyan: Caspr, magenta: Kv1.2.
h Quantification of the frequency of paranodal abnormalities (unwinding of Caspr and invasion of Kv1.2 into paranodes) in large- and small-diameter axons. Two-way ANOVA with multiple comparisons. Large diameter: $t = 6.293$, DF = 18.00, N = 5; small diameter: $t = 0.9374$, DF = 18.00, N = 6. Data are plotted as Mean±SEM. Each data point represents an individual animal. All p-values are labeled on the graphs. Source data are provided as a Source Data file.
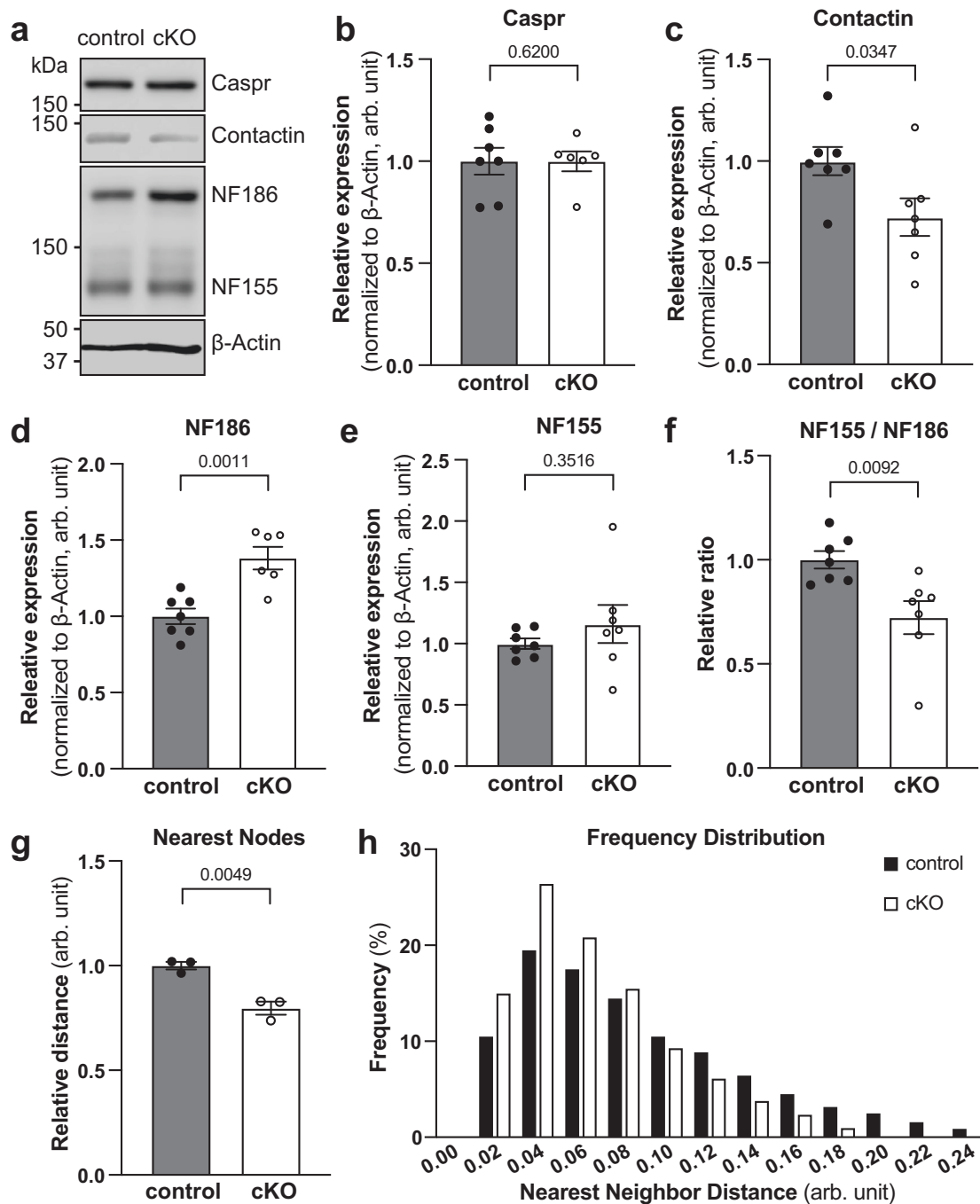
Fig. 2 | Loss of paranodal AnkG leads to more nodes of Ranvier. a Immunoblot of paranodal components Caspr, Contactin, and Neurofascin in whole spinal cord homogenates from 14 month-old control and cKO mice (run on 6% SDS-PAGE). β-Actin is used as the loading control (run separately on 14% SDS-PAGE). **b-e** Densitometry analysis of relative expression of Caspr (**b**), Contactin (**c**), NF186 (**d**) and NF155 (**e**) in the spinal cord of control and cKO mice. N = 7 for each genotype unless otherwise stated. Caspr: Unpaired t-test with 1 outlier in cKO is removed, two-tailed. $t = 0.008603$, DF = 11; Contactin: Unpaired t-test, two-tailed. $t = 2.380$, DF = 12; NF186: Unpaired t-test with 1 outlier in cKO removed, two-tailed. $t = 4.376$, DF = 11; NF155: Unpaired t-test with Welch's correction, two-tailed. $t = 0.9990$,

DF = 6.887. **f** Quantification of the ratio of NF155 to NF186 in the spinal cord of 14 month-old control and cKO mice. N = 7 for each genotype. Unpaired t-test, two-tailed. $t = 3.099$, DF = 12. **g** Nearest neighbor analysis of nodes of Ranvier in the optic nerve of 14 month-old control and cKO mice. N = 3 for each genotype. Unpaired t-test, two-tailed. $t = 5.629$, DF = 4. **h** Frequency distribution of distance between nearest nodes of Ranvier in the optic nerve of 14 month-old control and cKO mice. $n = 7703$ nodes from 3 control mice, and $n = 13096$ nodes from 3 cKO mice. Data are plotted as Mean±SEM. Each data point represents an individual animal. All p-values are labeled on the graphs. Source data are provided as a Source Data file.

fast conducting axons in the optic nerve[26]. We observed a dispersion of the CAP trace from AnkG cKO mice (Fig. 4a), a decrease in maximum conduction velocity (Fig. 4b), and reduced conduction velocity for each subgroup of axons (Fig. 4c). We conclude the thinner myelin and disrupted paranodal junctions explain the reduced conduction velocities[6,27] in aged AnkG cKO mice.

AnkG cKO mice show astrogliosis and Purkinje cell death

To determine the impact of PNJ disruption in older adult AnkG cKO mice, we examined glial and neuronal cell markers throughout the CNS, including the optic nerve, brain, and spinal cord. We observed a 2-fold increase in the fluorescence intensity of GFAP signal in the white matter of 14 month-old spinal cord (Fig. 5a, b), suggesting reactive
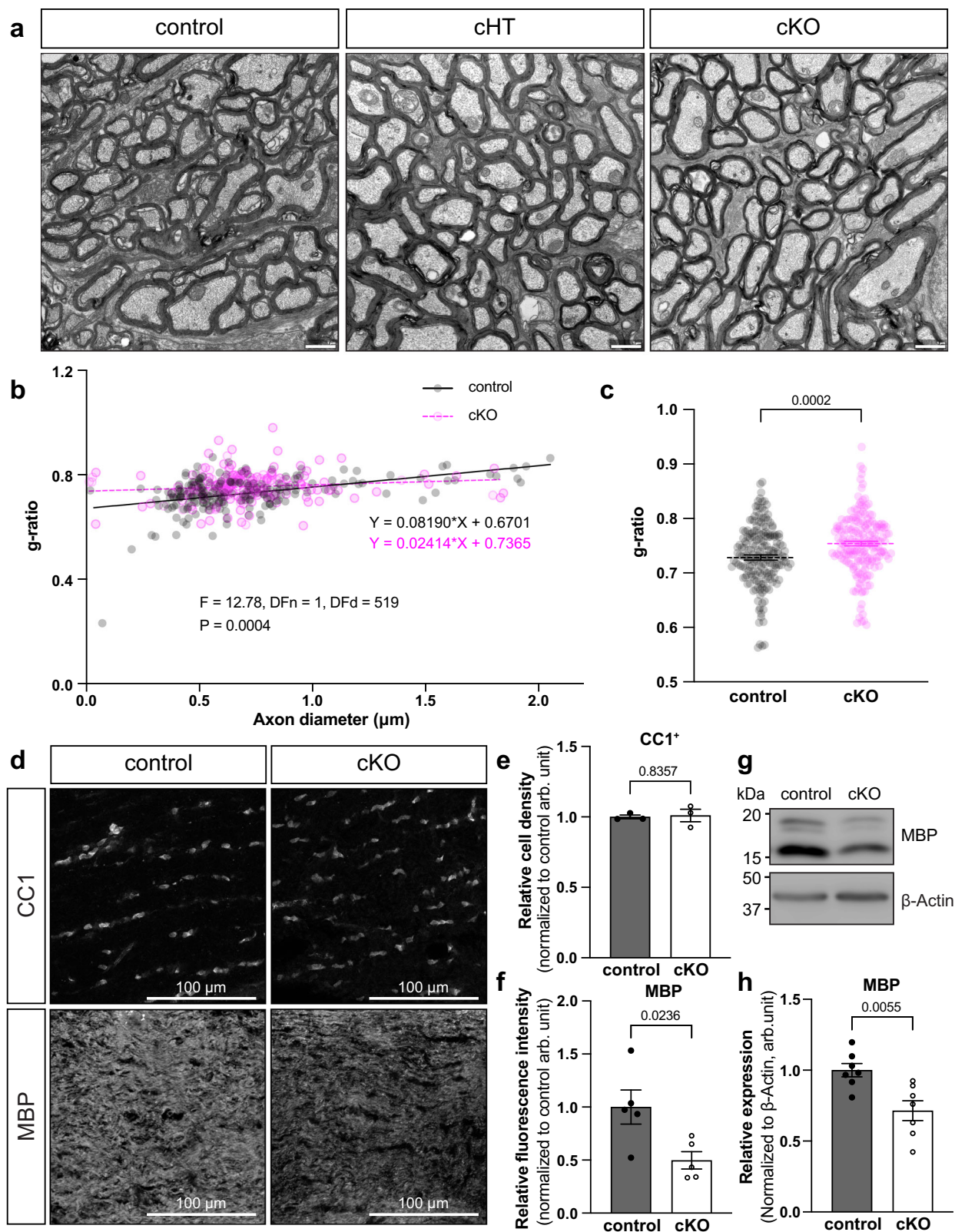
astrogliosis. This is further supported by immunoblotting of GFAP in the whole spinal cord homogenates from 14 month-old AnkG cKO and control mice (Fig. 5c).

Proper myelination and axoglial interactions are crucial for neuronal functions. Loss of myelin and disruption of PNJs are frequently associated with axonal injury and neurodegeneration. One particularly susceptible type of neuron is the cerebellar Purkinje neuron. For

example, both Caspr KO and NF155 KO mice show profound degeneration of Purkinje neuron axons, even in very young mice[27,28]. Thus, we further examined the effect of PNJ disruption on Purkinje neurons in oligodendroglial AnkG cKO mice. We observed a striking loss of Purkinje neurons in the anterior and central cerebellar lobules in the 14 month-old AnkG cKO mice, including lobules IV, V, VI, and VII (Fig. 5d). Quantitative analysis of the density of Calbindin+ cells along the

Fig. 3 | Loss of oligodendroglial AnkG leads to thinner myelin. a Representative images of transmission electron microscopy (TEM) analysis in the optic nerves of 16 month-old control, cHT and cKO mice. Scale bar, 1 μm. For each animal, more than 15 images were analyzed. **b** Scatter plot of g-ratio with axon diameter. Each data point represents an individual axon. $n = 193$ axons from one control and 187 axons from one cKO mice. Simple linear regression. **c** Quantification of g-ratio of axons in the optic nerves of 16 month-old control and cKO mice. Data are plotted as Mean±SEM. Each data point represents an individual axon. $n = 191$ axons from one control and 186 axons from one cKO mice. Two outliers from control and one outlier from cKO are excluded. Unpaired t-test, two-tailed. $t = 3.708$, DF = 375. **d** Immunostaining of CC1$^+$ mature oligodendrocytes and myelin basic protein (MBP) in the optic nerve of 14 month-old control and cKO mice. Scale bar, 100

μm. **e** Quantification of relative density of CC1$^+$ oligodendrocytes in the optic nerve of 14 month-old control and cKO mice. N = 3 for each genotype. Unpaired t-test, two-tailed. $t = 0.2213$, DF = 4. **f** Quantification of relative fluorescence intensity of MBP in the optic nerve of 14 month-old control and cKO mice. N = 5 for each genotype. Unpaired t-test, two-tailed. $t = 2.788$, DF = 8. **g** Immunoblot of whole spinal cord homogenates from 14 month-old control and cKO mice. β-Actin is used as the loading control (14% SDS-PAGE). **h** Densitometry analysis of relative expression of MBP in the spinal cord of 14 month-old control and cKO mice. N = 7 for each genotype. Unpaired t-test, two-tailed. $t = 3.374$, DF = 12. Data are plotted as Mean±SEM. Each data point represents an individual animal. Source data are provided as a Source Data file.
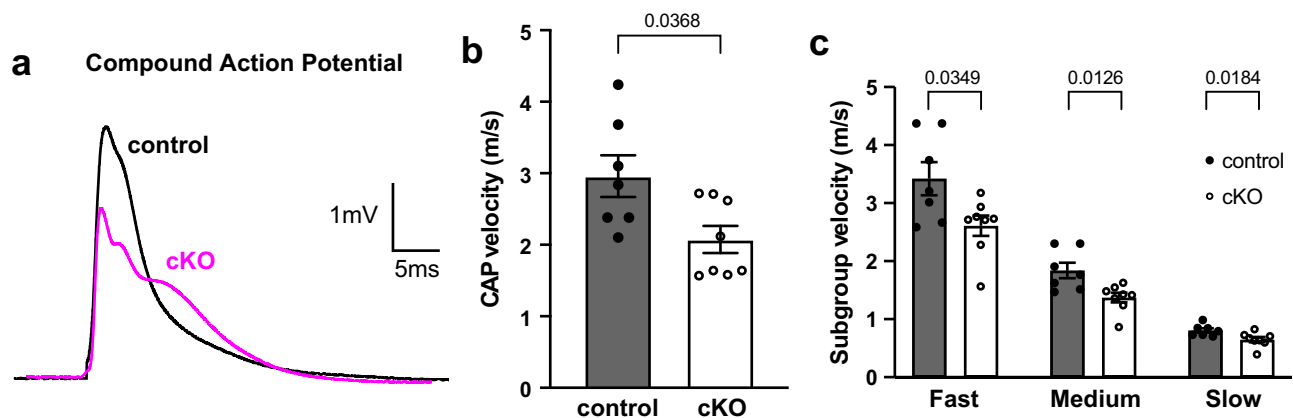
Fig. 4 | Loss of oligodendroglial AnkG results in slower conduction velocity of compound action potential. a Representative compound action potential (CAP) traces recorded from freshly dissected 14 month-old optic nerves with suction electrodes ex vivo. Black: control, Magenta: cKO. **b** The overall CAP velocity is calculated using the following formula: $V_{CAP} = Length\ of\ optic\ nerve\ /\ (T_{Vmax} − T_{VO})$. N = 7 for control, N = 8 for cKO. Mann-Whitney test, two-tailed. U = 10. **c** Three Gaussian curves are fitted under each trace to differentiate fast-, medium- and

slow-conducting axons. cKO optic nerves show a slower conduction velocity in all three groups of axons. N = 7 for control, N = 8 for cKO. Two-way ANOVA with multiple comparisons. Fitted Gaussian curve #1: $t = 2.435$, DF = 10.10; #2: $t = 3.012$, DF = 10.35; #3: $t = 2.698$, DF = 12.85. Data are plotted as Mean±SEM. Each data point represents an individual optic nerve. All p-values are labeled on the graphs. Source data are provided as a Source Data file.

Purkinje cell layer revealed a significant ~44% reduction of total Purkinje cells in 14 month-old AnkG cKO mice compared to control mice (Fig. 5e). Consistent with these histological observations, immunoblotting of Calbindin from whole cerebellum homogenates also showed a reduction in the 14 month-old AnkG cKO mice compared to control mice (Fig. 5f). Together, these results show that paranodal AnkG is required for proper CNS myelination, paranode integrity, and Purkinje neuron survival.

Loss of AnkG from oligodendrocytes reduces survival and overall health

The histological and physiological alterations in aged AnkG cKO mice suggested that the overall health and behavior of AnkG cKO mice could be impaired. To evaluate the overall health of the animals, we first examined postnatal survival rate. The Chi-square test showed a significant deviation of the AnkG cKO mice that are alive at P21 from the expected value based on the Mendelian ratio (Fig. 6a). Furthermore, both male and female AnkG cKO mice are significantly smaller in size and body weight compared to littermate controls starting from 20 weeks of age (Fig. 6b, c). As a result, AnkG cKO mice exhibited a shortened stride, stance, and sway in their gait patterns compared to littermate controls (Fig. 6d–g).

AnkG cKO mice have reduced locomotion

Since 14 month-old AnkG cKO mice have significantly fewer Purkinje neurons, we investigated their motor function. We performed the open field test in 30-50 week-old cKO male and female mice and compared them to control mice (Fig. 6h). We observed a significant

decrease in the total distance traveled by AnkG cKO mice of both sexes (Fig. 6i), but no difference in the time spent in the inner zone (Fig. 6j). Thus, aged AnkG cKO mice have impaired locomotion.

AnkG cKO mice have altered anxiety, social activity, and learnt helplessness behaviors

Myelin abnormalities and reduced white matter volume have been reported in patients with BD and SCZ[29,30]. To determine whether loss of oligodendroglial AnkG is sufficient to cause behavioral abnormalities, we performed a battery of tests examining anxiety, depression-like behaviors, sociability, and learning and memory in both male and female mice. Using an elevated plus maze, we examined anxiety of AnkG cKO versus littermate control mice (Fig. 7a). AnkG cKO mice spent significantly more time exploring the open arm compared to control mice (Fig. 7b), suggesting that loss of glial AnkG has a strong anxiolytic effect, similar to the mania-like behaviors observed in previous studies of mice with altered AnkG expression in neurons[21,22], and impaired threat/stress signal processing in humans with *ANK3* variants[31].

To determine the sociability and response to social novelty of AnkG cKO mice, we used the three-chamber test (Fig. 7c). Interestingly, AnkG cKO mice showed significantly higher preference to mice than empty cups (Fig. 7d). However, AnkG cKO mice demonstrate normal social novelty with comparable level of preference towards "stranger" mice to familiar compared to control mice (Fig. 7e).

Bipolar disorder in humans manifests as oscillating episodes of both mania and depression. To test whether AnkG cKO mice exhibit behavioral abnormalities related to depression, we performed the
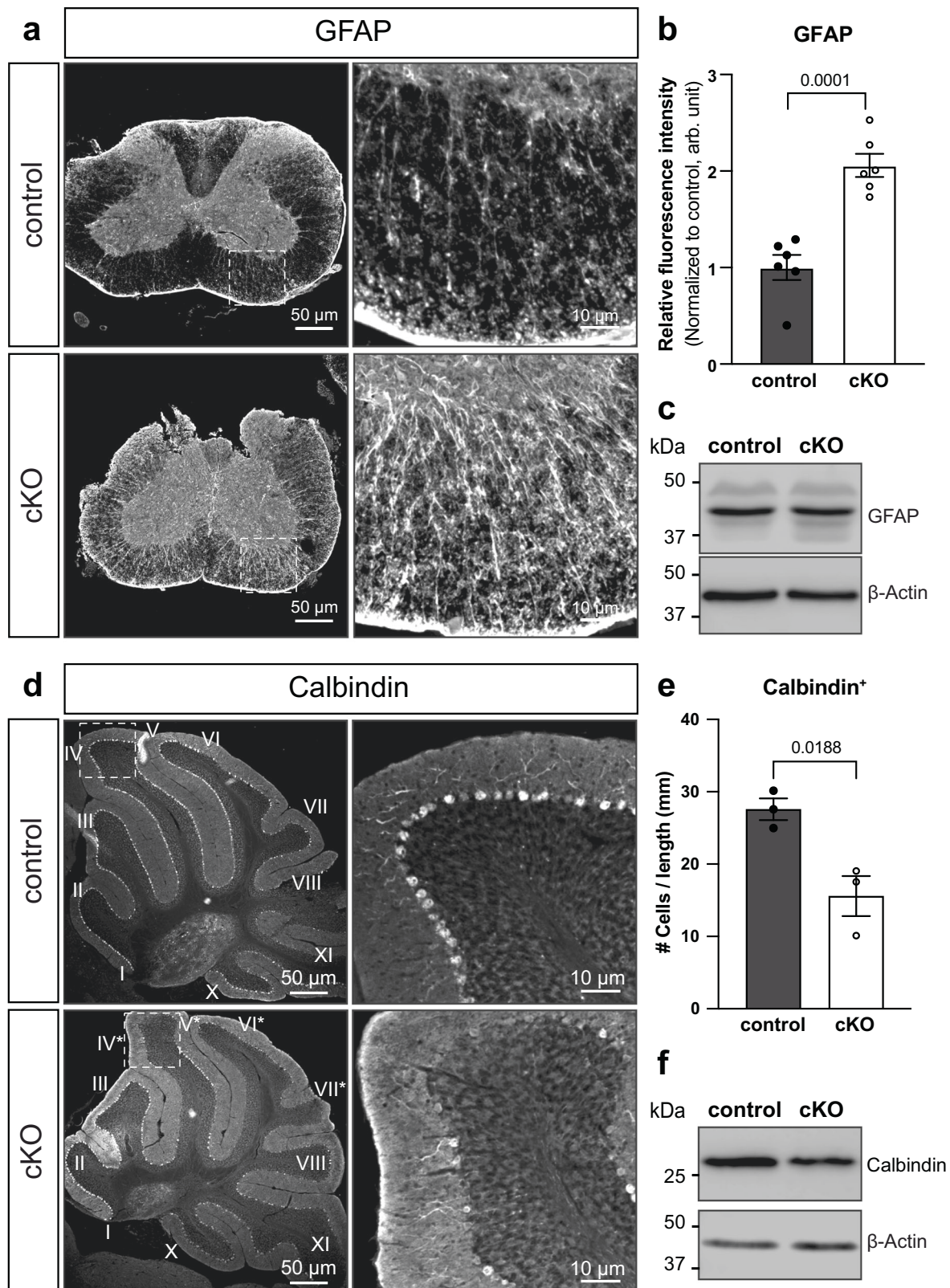
forced swim test (FST) and tail suspension test (TST). Surprisingly, AnkG cKO adults were unable to swim regardless of age, precluding the evaluation of depression-like behaviors using FST. However, during the TST test (Fig. 7f), AnkG cKO mice spent significantly more time struggling compared to control mice, suggesting a lowered level of learnt helplessness behavior in AnkG cKO mice.

To determine whether AnkG cKO mice have learning and memory defects, we performed the contextual fear conditioning test (Fig. 7g). During the training phase, AnkG cKO mice exhibited a significantly higher percentage of freezing behavior immediately after the foot shock compared to control mice (Fig. 7h). However, their ability to recall the stressful events 24 hours post training remained similar to

Fig. 5 | Disruption of paranodal junction and myelination leads to astrogliosis and Purkinje cell death in AnkG cKO mice. a Immunofluorescence staining of GFAP in the spinal cord of 14 month-old control and cKO mice. Scale bar, 50 μm. White matter region is zoomed in on the right. Scale bar, 10 μm. **b** Quantification of relative fluorescence intensity of GFAP in the spinal cord of 14 month-old control and cKO mice. N = 6 for each genotype. Unpaired t-test, two-tailed. $t = 5.968$, DF = 10. **c** Immunoblot of GFAP in the whole spinal cord homogenates of 14 month-old control and cKO mice. β-Actin is used as loading control. Experiments are repeated three times. **d** Immunofluorescence staining of Calbindin in the cerebellum of 14

month-old control and cKO mice. I – X label each lobule of the cerebellum. Asterisks indicate lobules with significant Purkinje cell death. Scale bar, 50 μm. Lobule IV is zoomed in on the right. Scale bar, 10 μm. **e** Quantification of Purkinje neuron density. N = 3 for each genotype. Unpaired t-test, two-tailed. $t = 3.819$, DF = 4. **f** Immunoblot of Calbindin in the cerebellar homogenates of 14 month-old control and cKO mice. β-Actin is used as loading control. Experiments are repeated three times. Data are plotted as Mean±SEM. Each data point represents an individual animal. All p-values are labeled on the graphs. Source data are provided as a Source Data file.

control mice (Fig. 7h). Together, these results suggest that AnkG cKO mice have heightened social activity, but normal learning and memory.

Inducible loss of oligodendroglial AnkG in young adult mice has mild effects

We previously showed that loss of AnkG delays the developmental assembly of paranodes[15]. However, the effect of such a delay is limited to the perinatal stage. To further uncouple pathologies in the adult from disruption of paranodes during early development, we generated inducible oligodendroglial conditional *Ank3* knockout mice (*NG2^CreERTM; Ank3^F/F*, AnkG icKO mice). Tamoxifen was injected into 2 month-old adult mice, long after the PNJs were formed (Fig. 8a). After 1 month of recombination, we confirmed efficient and specific deletion of paranodal AnkG from the optic nerve (Fig. 8b-c). Despite the loss of paranodal AnkG (Fig. 8b-c, **arrowheads**), 3 month-old AnkG icKO mice had no defects in their PNJs in the optic nerve (Fig. 8d-e) since both Caspr and Kv1 channels were properly clustered at paranodes and juxtaparanodes, respectively.

To compare the AnkG icKO with AnkG cKO mice, we performed a battery of behavioral tests in AnkG icKO young adult mice. We found that loss of AnkG from young adult oligodendrocytes had minimal effects on health and behavior, including body weight (Fig. 8f), gait patterns (Fig. 8g–i), and locomotion (Fig. 8j, k). AnkG icKO mice demonstrated a mild defect in latency to fall from the rotarod (Fig. 8l). Performance on the elevated plus maze in AnkG icKO remained unchanged compared to control mice (Fig. 8n). AnkG icKO mice also showed comparable levels of social interactions compared to control mice (Fig. 8o, p). We found a modest, but significant, reduction in learnt helplessness behavior characterized by time spent being immobile during the tail suspension test (Fig. 8m). Since complex behaviors are orchestrated by many brain circuits that are already formed in young adults, our data suggest that the PNJ and myelination may be more important during the development of the responsible circuits rather than their maintenance in young adults.

Translatomic profiling reveals compensatory molecular machineries that may maintain axoglial interactions in adults

In the absence of strong behavioral defects in the AnkG icKO mice, we sought to identify compensatory mechanisms that might contribute to preservation of the PNJ and oligodendrocyte function. Therefore, we performed unbiased translatomic profiling of oligodendrocytes from the whole brain homogenate of *NG2^CreERTM; Ank3^F/F; Rpl22^HA/+* (AnkG icKO RiboTag) versus *NG2^CreERTM; Rpl22^HA/+* (control RiboTag) mice (Fig. 9a). This experiment reveals the mRNA transcripts actively engaged with ribosomes in mutant and control oligodendrocytes. Following tamoxifen injection and Cre-mediated recombination, we successfully expressed HA-epitope tagged ribosomes in NG2+ cells (Fig. 9b). Quantitative real-time PCR (qPCR) further confirmed ~8-fold enrichment of the oligodendrocyte lineage-specific transcript *Olig2*, and ~75% decrease of the astrocytic transcript *Aldh1l1* and the neuronal transcript *NeuN* following immunoprecipitation (Fig. 9c). Moreover, the oligodendroglial isoforms of AnkG (190 kDa and 270 kDa) were both over-represented in our immunoprecipitated (IP) samples compared to the crude extract (input), while the neuronal specific isoform

(480 kDa) was significantly reduced after IP (Fig. 9d). These results are consistent with our previous study[15] and confirms the efficiency and specificity of the RiboTag system.

Among the differentially regulated genes, we observed a general reduction of many myelin-related transcripts (Fig. 9e, blue) in AnkG icKO RiboTag mice compared to control RiboTag mice, including *Mal* (Myelin and lymphocyte protein), *Ptgds* (Prostaglandin D2 synthase), *Mobp* (Myelin-associated oligodendrocyte basic protein), *Mbp* (Myelin basic protein), *Plp1* (Proteolipid protein 1), *Tspan2* (Tetraspanin 2), *Cldn11* (Claudin 11), and *Opalin* (Oligodendrocytic myelin paranodal and inner loop protein), among others (Fig. 9e and Supplementary Data File 1). These translatomic changes are consistent with our observations in the histological and biochemical analyses using antibodies against MBP (Fig. 3d, f–h) and the reduced myelin thickness as determined by electron microscopy (Fig. 3a–c). These data strongly suggest that oligodendroglial AnkG is important for proper myelination of the CNS.

On the other hand, among the significantly upregulated genes (Fig. 9e, magenta), we also found a consistent increase in transcripts encoding the actin-spectrin-ankyrin cytoskeletal network, including *Sptan1* (αII spectrin), *Sptb* (βI spectrin), *Sptbn1* (βII spectrin), *Sptbn2* (βIII spectrin), *Actn2* (αII actinin), *Actn4* (αIV actinin), and *Ank2* (AnkyrinB, AnkB). To further validate these translational changes on the protein level, we performed immunoblotting using antibodies against some of the candidates, and we detected elevated level of αII, βII, and βIII spectrins, as well as AnkB in the cKO whole brain homogenate compared to control at 14 months-of-age (Fig. 9f). These results strongly suggest that compensation by AnkB and its binding partners, as well as the subsequent cytoskeletal remodeling, may partially rescue axoglial interactions in the absence of AnkG.

To further confirm the upregulated AnkB is found at paranodes, we performed immunofluorescence labeling of AnkB together with the nodal marker βIV spectrin (Fig. 9g, h). 6 month-old AnkG cKO mice show clear enrichment of paranodal AnkB in the optic nerve compared to littermate control mice (Fig. 9g, open arrowheads). Interestingly, this phenomenon is seen in 14 month-old mice, with less obvious paranodal enrichment for AnkB (Fig. 9h). To further reveal the overall impact of AnkG deletion from oligodendrocytes, we performed gene ontology analyses of differentially expressed genes (Fig. 9i). Among all the downregulated cellular components (CC, blue, solid), we found a systemic reduction in mitochondrial respiratory chain, extracellular matrix, and actin cytoskeleton related genes. Furthermore, extracellular matrix binding, oxidation, actin binding, and myelin sheath components were also significantly reduced among all molecular functions (MF, blue outline). AnkG icKO RiboTag mice also had significant changes in opposition to the downregulated cellular components and molecular functions (Fig. 9i). For instance, the actin cytoskeleton, cell-substrate junction, focal adhesion, and myosin complex were all significantly enriched in the upregulated cellular components (CC, magenta, solid). As a result, the underlying molecular functions (MF, magenta outline) involving actin binding, extracellular matrix constituents, microfilament binding, cell adhesion molecule binding, spectrin binding, and actin-dependent ATPase and motor activity were also increased. That the actin cytoskeleton and
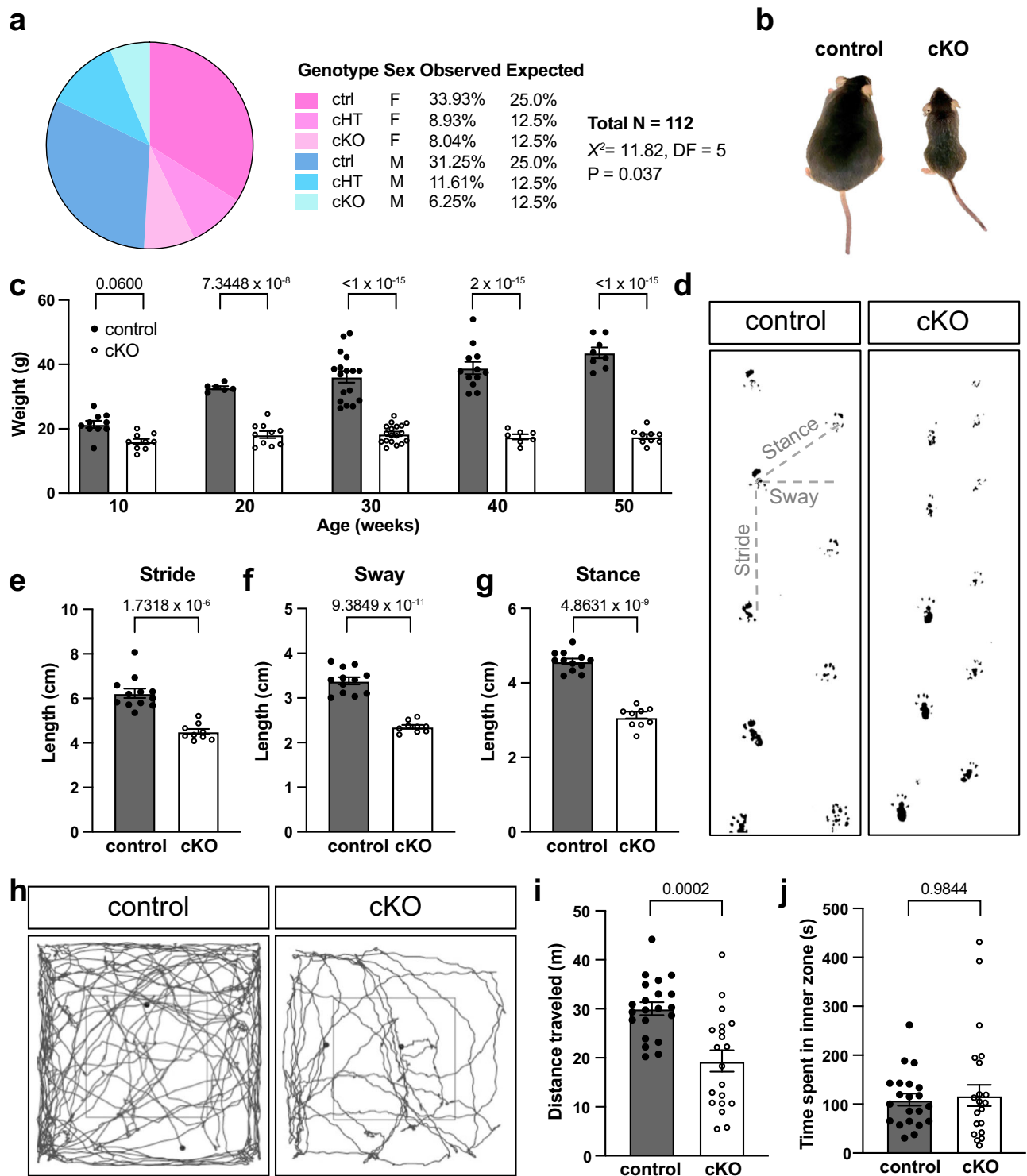
Fig. 6 | Loss of oligodendroglial AnkG is detrimental to survival, growth, and locomotion. a cKO mice show postnatal lethality with incomplete penetrance. Chi-square test, two-tailed. **b** A representative image of male 14 month-old control and cKO mice. **c** Quantification of body weight in both sexes. Two-way ANOVA with multiple comparisons. 10 weeks: $t = 2.551$, DF = 96.00, N = 10 for control, N = 9 for cKO; 20 weeks: $t = 6.192$, DF = 96.00, N = 6 for control, N = 10 for cKO; 30 weeks: $t = 11.46$, DF = 96, N = 17 for control, N = 18 for cKO; 40 weeks: $t = 9.857$, DF = 96.00, N = 12 for control, N = 7 for cKO; 50 weeks: $t = 11.74$, DF = 96.00, N = 8 for control, N = 9 for cKO. **d** Representative image of hind-foot prints for gait analysis. **e**–**g** Quantification of stride (**e**), sway (**f**), and stance (**g**) in mice older than 40 week-old of both sexes. N = 12 for control, N = 9 for cKO. Stride: Unpaired t-test with Welch's correction, two tailed. $t = 7.179$, DF = 16.66; Sway: Unpaired t-test with Welch's correction, two tailed. $t = 11.22$, DF = 16.17; Stance: Unpaired t-test, two-tailed. $t = 12.74$, DF = 19. **h** Representative track plots showing the center of 40 week-old male mice during a 10-minute open field test. **i** Quantification of distance traveled by both sexes (30 to 50 week-old). N = 21 for control, N = 20 for cKO. Unpaired t-test with Welch's correction, two-tailed. $t = 4.201$, DF = 31.21. **j** Quantification of time spent in the inner zone. N = 21 for control, N = 20 for cKO. Whitney test, two-tailed. U = 209. Data are plotted as Mean±SEM. Each data point represents an individual animal. All p-values are labeled on the graphs. Source data are provided as a Source Data file.
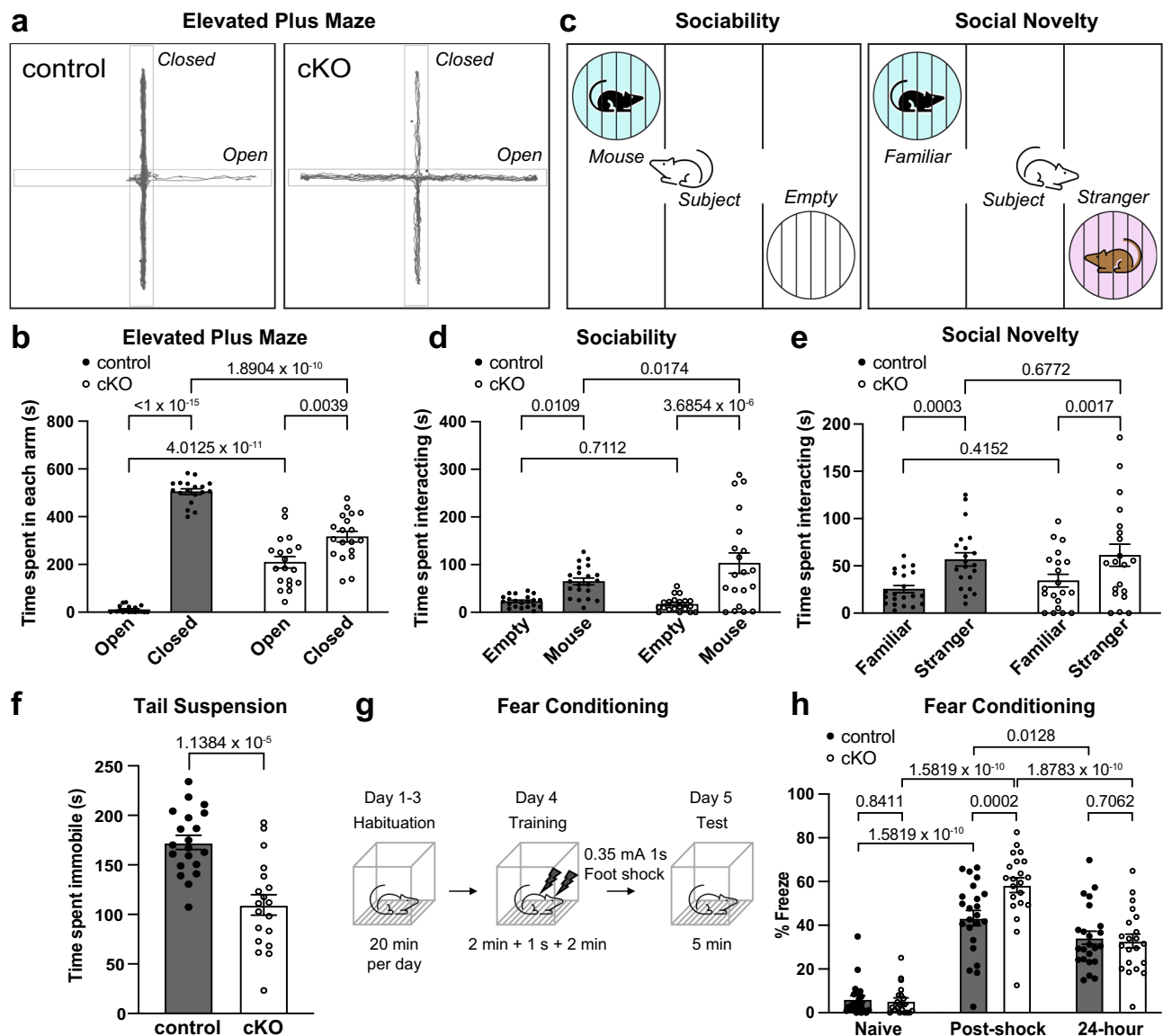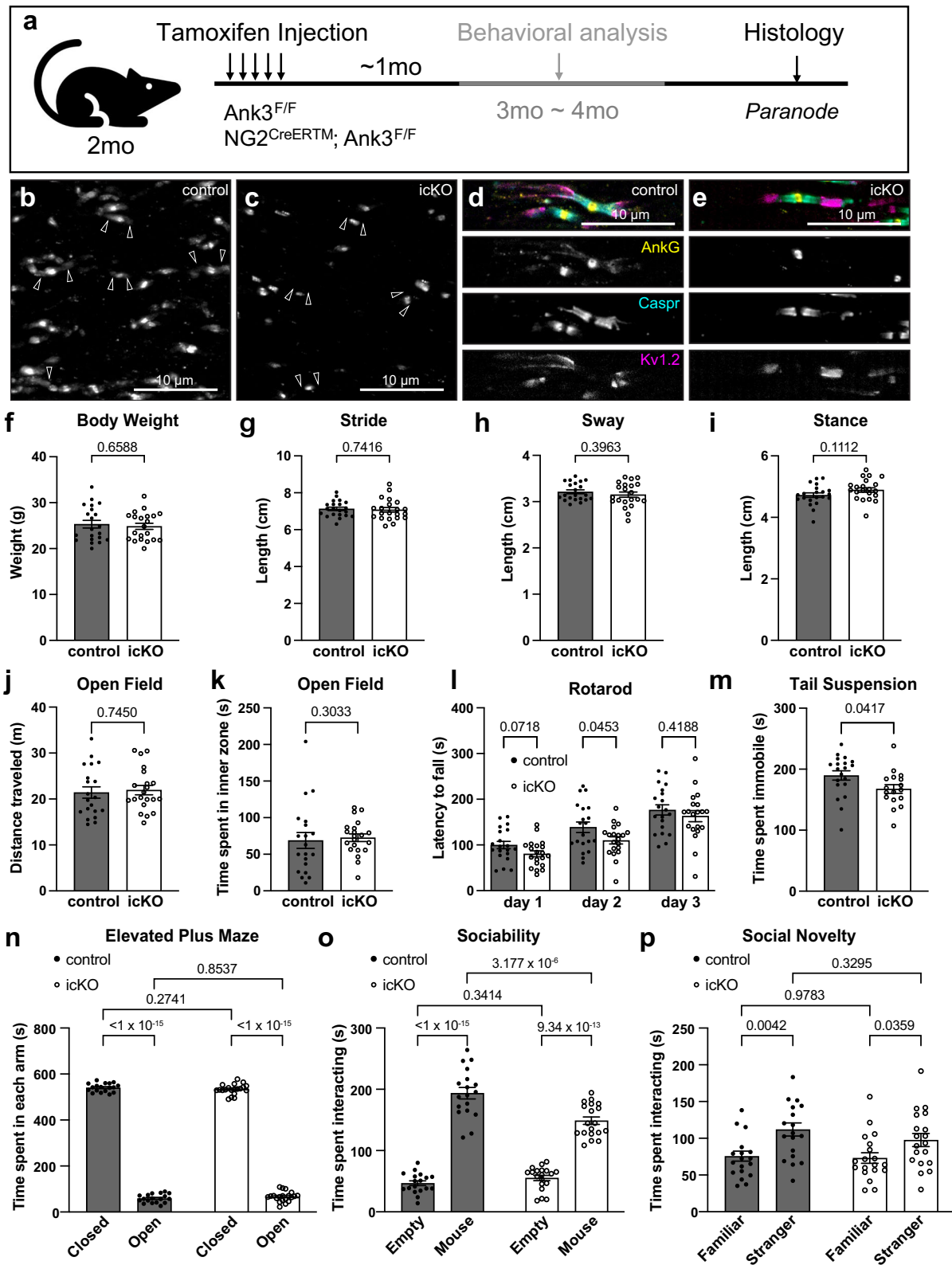
Fig. 7 | Loss of oligodendroglial AnkG leads to altered sociability, anxiety, and learnt helplessness. a Representative track plots showing the position of the center of the animal during a 10-minute elevated plus maze test. Left: 50 week-old female control mouse. Right: 50 week-old female cKO mouse. **b** Quantification of total time spent in the open arms by both male and female control and cKO mice that are between 30 and 50 week-old. N = 18 for control, N = 19 for cKO. Two-way ANOVA with multiple comparisons. control$_{open}$ vs control$_{closed}$: t = 13.90, DF = 35.00; cKO$_{open}$ vs cKO$_{closed}$: t = 3.089, DF = 35.00; control$_{open}$ vs cKO$_{open}$: t = 7.814, DF = 70.00; control$_{closed}$ vs cKO$_{closed}$: t = 7.448, DF = 70.00. **c** Illustration of three-chamber social tests for sociability and social novelty. **d** Quantification of sociability of both male and female control and cKO mice that are between 30- and 50 week-old by time spent interacting with mouse versus empty cage. N = 21 for control, N = 20 for cKO. Two-way ANOVA with multiple comparisons. control$_{empty}$ vs control$_{mouse}$: t = 2.675, DF = 39.00; cKO$_{empty}$ vs cKO$_{mouse}$: t = 5.386, DF = 39.00; control$_{empty}$ vs cKO$_{empty}$: t = 0.3716, DF = 78.00; control$_{mouse}$ vs cKO$_{mouse}$: t = 2.429,

DF = 78.00. **e** Social novelty measured by time spent with stranger versus familiar mice. N = 21 for control, N = 20 for cKO. Two-way ANOVA with multiple comparisons. control$_{familiar}$ vs control$_{stranger}$: t = 4.0090, DF = 39.00; cKO$_{familiar}$ vs cKO$_{stranger}$: t = 3.365, DF = 39.00; control$_{familiar}$ vs cKO$_{familiar}$: t = 0.8191, DF = 78.00; control$_{stranger}$ vs cKO$_{stranger}$: t = 0.4179, DF = 78.00. **f** Quantification of immobility during the tail suspension test. N = 20 for control, N = 19 for cKO. Unpaired t-test, two-tailed. t = 5.069, DF = 37. **g** Illustration of contextual fear conditioning test for learning and memory. **h** Percentage of time spent freezing. N = 23 for control, N = 21 for cKO. Two-way ANOVA with multiple comparisons. control$_{naïve}$ vs cKO$_{naïve}$: q = 0.284, DF = 126.0; control$_{post-shock}$ vs cKO$_{post-shock}$: q = 5.370, DF = 126.0; control$_{24-hour}$ vs cKO$_{24-hour}$: q = 0.534, DF = 126.0. control$_{naïve}$ vs control$_{post-shock}$: q = 16.987, DF = 84.00; control$_{post-shock}$ vs control$_{24-hour}$: q = 4.111, DF = 84.00; cKO$_{naïve}$ vs cKO$_{post-shock}$: q = 23.161, DF = 84.00; cKO$_{post-shock}$ vs cKO$_{24-hour}$: q = 11.164, DF = 84.00. All data are plotted as Mean±SEM. Each data point represents an individual animal. Source data are provided as a Source Data file.

extracellular matrix molecular functions are present in both the downregulated and upregulated pathways suggests these are redundant and compensatory molecular functions that maintain paranodal axoglial interactions after loss of glial AnkG. Overall, our unbiased translatomic profiling of AnkG icKO RiboTag mice strongly supports the conclusion that oligodendroglial AnkG regulates axoglial interactions at the paranode and identifies redundant and compensatory pathways that may also function to maintain axon-glia interactions.

Discussion

Loss of neuronal AnkG contributes to bipolar-like behavioral abnormalities in mice[21,22]. Since AnkG is the master regulator of neuronal polarity, and its functions at the AIS and nodes of Ranvier in neurons are well understood[3,32], it has been assumed that neuronal dysfunction underlies the BD-like behaviors in mice. However, AnkG has a comparable expression level in oligodendrocytes, but its roles in these glial cells are much less understood. Thus, we hypothesized that

a Tamoxifen Injection · Behavioral analysis · Histology; 2mo; Ank3$^{F/F}$, NG2^{CreERTM}; Ank3$^{F/F}$; ~1mo; 3mo ~ 4mo; Paranode

b control, **c** icKO, **d** control, **e** icKO (AnkG, Caspr, Kv1.2), 10 μm scale bars

f Body Weight (0.6588), **g** Stride (0.7416), **h** Sway (0.3963), **i** Stance (0.1112)

j Open Field (0.7450), **k** Open Field (0.3033), **l** Rotarod (day 1: 0.0718, day 2: 0.0453, day 3: 0.4188), **m** Tail Suspension (0.0417)

n Elevated Plus Maze, **o** Sociability, **p** Social Novelty

glial AnkG may also contribute to animal behavior. Here, we addressed three important questions: 1) is glial AnkG important for neuron-glia interactions, 2) is disruption of glial AnkG sufficient to alter the physiology and behaviors of mice, and 3) what molecular pathways are altered in the absence of glial AnkG? By generating oligodendroglial specific AnkG knockout animals, we explored the histological, physiological, behavioral, molecular, and biochemical features of these mice, and we showed the importance of oligodendroglial AnkG in aged

animals. This study further highlights the pleotropic effects of AnkG in different cell types, at different developmental stages, as well as the potential contribution of glial *ANK3* to neuropsychiatric disorders like BD.

The PNJs are the largest junctional adhesion complex in vertebrates. Maintaining their structural integrity is pivotal to an efficient and functional nervous system across all myelinated organisms. Nodes of Ranvier are assembled through two overlapping glial mechanisms

Fig. 8 | Loss of AnkG from adult mice causes mild deficits. a Illustration of inducible loss of AnkG from oligodendrocytes in *NG2^CreERTM^;Ank3 ^F/F^* mice (AnkG icKO). **b-c** Immunofluorescence staining of AnkG in the optic nerve of 3 month-old AnkG icKO mice (**b**) with littermate control (**c**). Experiments were performed three times. Scale bar, 10 μm. **d, e** Immunofluorescence staining in the optic nerve of 3 month-old AnkG icKO mice (**d**) with littermate control (**e**). Yellow: AnkG, Cyan: Caspr, Magenta: Kv1.2. **f** Body weight of AnkG icKO vs control mice. N = 21 for each genotype. Unpaired t-test, two-tailed. $t = 0.4449$, DF = 40. Experiments were performed three times. Scale bar, 10 μm. **g-I** Gait analyses of AnkG icKO vs control mice. N = 21 for each genotype. Stride: Unpaired t-test, two-tailed. $t = 0.3321$, DF = 40; Sway: Mann-Whitney test, two-tailed. U = 186; Stance: Unpaired t-test, two-tailed. $t = 1.629$, DF = 40. **j, k** Open field test. N = 20 for control, N = 21 for icKO. Distance traveled: Unpaired t-test, two-tailed. $t = 0.3275$, DF = 39; Time in inner zone: Mann-Whitney test, two-tailed. U = 170. **l** Latency to fall from the accelerating rotarod. N = 20 for each genotype. Two-way ANOVA with multiple comparisons. control vs icKO day1: $t = 1.854$, DF = 36.46. day2: $t = 2.079$, DF = 33.45. day3:

$t = 0.8175$, DF = 37.76. **m** Immobility during the suspension test. N = 20 for control, N = 17 for icKO. Unpaired t-test, two-tailed. $t = 2.114$, DF = 35. **n** Time spent in open and closed arms during the elevated-plus-maze test. N = 18 for control, N = 20 for icKO. Two-way ANOVA with multiple comparisons. control$_{closed}$ vs control$_{open}$: $t = 71.11$, DF = 72.00. icKO$_{closed}$ vs icKO$_{open}$: $t = 71.11$, DF = 72.00. control$_{closed}$ vs icKO$_{closed}$: $t = 1.102$, DF = 72.00. control$_{open}$ vs icKO$_{open}$: $t = 1.102$, DF = 72.00. **o** Three-chamber test of sociability. N = 18 for control, N = 19 for icKO. Two-way ANOVA with multiple comparisons. control$_{empty}$ vs control$_{mouse}$: $t = 16.603$, DF = 35.00, $p < 1 \times 10^{-15}$. icKO$_{empty}$ vs icKO$_{mouse}$: $t = 10.861$, DF = 35.00. control$_{empty}$ vs icKO$_{empty}$: $t = 0.958$, DF = 70.00. control$_{mouse}$ vs icKO$_{mouse}$: $t = 5.065$, DF = 70.00. **p** Three-chamber test of social novelty. N = 18 for control, N = 19 for icKO. Two-way ANOVA with multiple comparisons. control$_{familiar}$ vs control$_{stranger}$: $t = 3.066$, DF = 35.00. icKO$_{familiar}$ vs icKO$_{stranger}$: $t = 2.182$, DF = 35.00. familiar$_{control}$ vs icKO$_{control}$: $t = 0.027$, DF = 70.00. control$_{stranger}$ vs icKO$_{stranger}$: $t = 0.982$, DF = 70.00. Data are plotted as Mean±SEM. Data points represent an individual animal. Source data are provided as a Source Data file.

that converge on the axonal cytoskeleton[5]. In the CNS, the axoglial-dependent assembly of the PNJ cytoskeleton is the primary node assembly mechanism, with a second mechanism that depends on a complex set of extracellular matrix molecules that can stabilize and retain nodal cell adhesion molecules for subsequent binding to axonal scaffolds and ion channels[25]. The intricate and overlapping systems for node assembly highlights the evolutionary significance of redundant regulatory mechanisms. Our study focused on the maintenance of axoglial junctions at the paranodes, which corroborates the same principle of increasing the safety factor to ensure an efficient and functional nervous system throughout life. Besides the role of the scaffolding protein AnkG in maintaining the PNJs, our unbiased translatomic profiling in oligodendrocytes in the absence of AnkG reveals both systemic remodeling of the spectrin-actin cytoskeletal network and dramatic changes in extracellular matrix components.

During aging, many developmental processes are re-employed to repair or replace damaged cells, tissues, and organs. Meanwhile, it is also a naturally perturbed system, where the extracellular environment, intercellular interactions, and intracellular properties of the aged cells are distinct from their developing counterparts. Therefore, aged animals provide a unique opportunity to further dissect out a well-compensated and complex system like the PNJs. In younger adult animals, we found the compensatory mechanisms are overwhelmingly effective, which could potentially mask the critical functions of proteins that normally contribute to paranode assembly. Here, we confirmed that in young AnkG cKO mice, AnkB may compensate for the loss of AnkG[15], but such compensation is not sufficient to maintain the deteriorating PNJ during aging. Previous studies showed that in aged CNS, paranodal reorganization results in the loss of transverse bands[33]. In AnkG cKO mice, such a process may be accelerated. In aged Caspr mutant mice, disruption of paranodal axoglial interactions causes axon degeneration and neuronal cell death[34]. Similarly, deletion of βII spectrin from glial cells slows AP conduction in sciatic nerves in aged but not young adults[24]. Based on these previous studies, we speculate that paranode structure is stable throughout early life due to compensatory mechanisms in AnkG cKO mice, however, these mechanisms are not sufficient to maintain the PNJs in aged AnkG cKO mice, perhaps due to lower affinity for the paranodal CAMs than their original interacting partners in control animals.

Notably, actin cytoskeleton remodeling has been shown to regulate myelin development and regeneration in both CNS and PNS[35,36]. The systemic change in the cytoskeletal network in response to loss of paranodal AnkG further highlights the contribution of the spectrin-actin cytoskeletal network to axoglial interactions[24]. Our translatomic data also show that AnkG might be important for the maturation of oligodendrocytes, as many markers of mature oligodendrocytes are significantly reduced in the absence of AnkG. However, we did not see significant changes in the number of mature oligodendrocytes
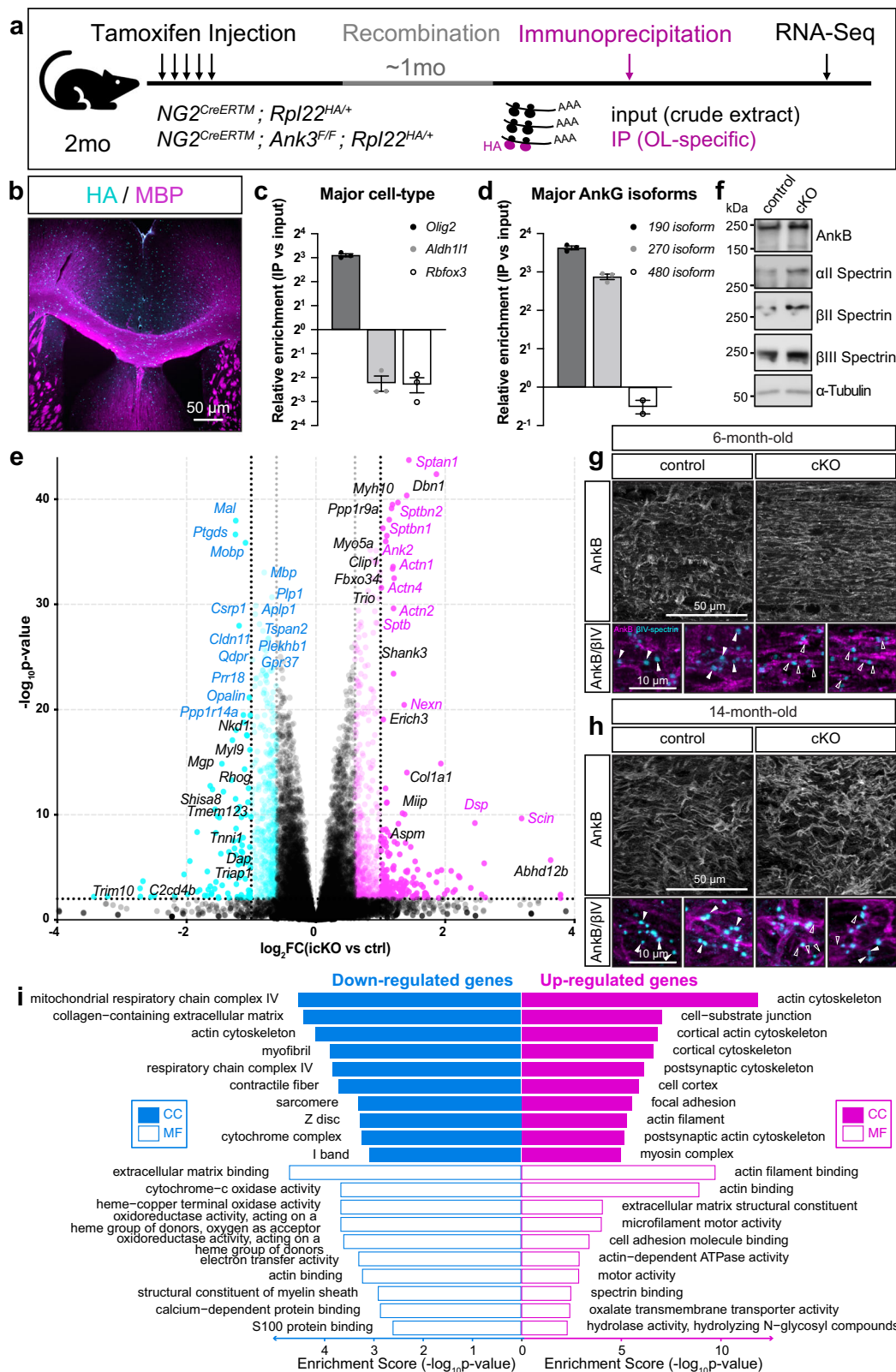
in aged AnkG cKO mice. This suggests that neither oligodendrocyte proliferation, differentiation, nor survival is disturbed. It is more likely that each mature oligodendrocyte produces less myelin-related proteins, forming myelin sheaths that are thinner and shorter in length. More experiments are needed in the future to examine this hypothesis.

We observed alterations in some behaviors in the aged AnkG cKO mice. This may be due to the susceptibility of large-diameter axons to the loss of paranodal AnkG. For instance, the death of Purkinje neurons is likely due to their relatively large size (50 - 80 μm) and high tonic activity. Interestingly, the Purkinje cell loss is restricted to the anterior and central lobules, which are known to be more susceptible to aging and perturbation by diseases, but not the posterior lobules which are naturally resistant to neurodegeneration[37–39]. Functionally, lobules IV/V/VI are heavily involved in not only motor coordination but also social behaviors[40,41], which potentially explains the behavioral alterations in AnkG cKO mice. Furthermore, at the translatomic level, we observed changes in genes associated with social activity (e.g. *Shank3*[42]) and depression (e.g. *Erich3*[43]). Interestingly, like *Ank3*, these genes are also expressed in both neurons and oligodendrocytes, with their neuronal functions better characterized than their glial functions.

Despite our best efforts, this work has several limitations. First, our analyses rely on the Cre-lox system, which has the potential risk of "leakiness" into non-targeted cells, as well as the potential for inefficient recombination. For instance, NG2 is expressed in pericytes in addition to oligodendroglial-lineage cells, which could potentially contribute to the effects we observed in these cKO mice. On the other hand, despite higher lineage-specificity, the tamoxifen induced *NG2^CreRTM^* mice have only 25-50% efficiency in deleting *Ank3*, depending on the brain region. Therefore, the dramatic differences between *NG2^Cre^* and *NG2^CreRTM^* mice could be due to the limitations of the current genetic tools. Furthermore, this study was not meant to create a mouse model that mimics human bipolar disorder, as it is a complex human disease. Therefore, our study only supports the conclusion that glial cells may contribute to the abnormal behaviors shown in BD patients. Interestingly, a recent study by Hughes et al. suggests that a rare SNP at the human *ANK3* locus might be protective against BD via the oligodendroglial isoform of AnkG[44]. Our experiments here establish a functional connection between glial AnkG and BD-like behaviors in mice. Nevertheless, the exact function of this particular human *ANK3* SNP remains to be tested. Future experiments with better tools will be needed to definitively address these remaining questions.

Methods

All experiments were performed in compliance with regulations by the Institutional Biosafety Committees (IBC) at Baylor College of Medicine and the Weizmann Institute of Science. All animal care and experimental procedures were conducted in compliance with the National

a Tamoxifen Injection | Recombination ~1mo | Immunoprecipitation | RNA-Seq

2mo · $NG2^{CreERTM}$; $Rpl22^{HA/+}$ · $NG2^{CreERTM}$; $Ank3^{F/F}$; $Rpl22^{HA/+}$ · input (crude extract) · IP (OL-specific)

b HA / MBP · 50 μm

c Major cell-type — Relative enrichment (IP vs input): Olig2, Aldh1l1, Rbfox3

d Major AnkG isoforms — Relative enrichment (IP vs input): 190 isoform, 270 isoform, 480 isoform

f control / cKO — AnkB, αII Spectrin, βII Spectrin, βIII Spectrin, α-Tubulin

e Volcano plot — $-\log_{10}$ p-value vs $\log_2 FC$ (icKO vs ctrl)

g 6-month-old — control / cKO — AnkB, AnkB/βIV · 50 μm · 10 μm

h 14-month-old — control / cKO — AnkB, AnkB/βIV · 50 μm · 10 μm

i Down-regulated genes / Up-regulated genes — Enrichment Score ($-\log_{10}$ p-value)

Animals

Mice were group-housed at Baylor College of Medicine on a 12 h/12 h light/dark cycle (lights on at 7:00 am), with room temperature maintain at 22 °C, humidity at 40–60%, and access to food and water *ad libitum*. All mice were regularly monitored by veterinary and animal care staff at the Center of Comparative Medicine. Both male and female mice were used in this study.

Oligodendroglial lineage specific AnkG conditional knockout mice (AnkG cKO) were generated by crossing $Ank3^{F/F}$ mice with $NG2^{Cre}$ mice. This results in the deletion of exons 22 and 23 and a premature

Fig. 9 | Translatomic profiling of AnkG-deficient oligodendrocytes reveals compensatory cytoskeletal mechanisms. a Illustration of the experimental design for translatomic profiling in NG2+ oligodendroglial-lineage cells. **b** Immunofluorescence staining of HA-tagged ribosome and MBP in the coronal brain section of a 3 month-old *NG2*^{CreERTM};RiboTag mouse. (Cyan: HA, Magenta: MBP). Experiments are performed in three animals. Scale bar, 50 μm. **c** Relative enrichment of major cell-type markers (oligodendrocytes: *Olig2*, astrocytes: *Aldh1l1*, neurons: *NeuN*) by HA-IP in *NG2*^{CreERTM};RiboTag mice. Data are plotted as Mean±SEM. Data points represent individual animals (N = 3). **d** Relative enrichment of major AnkG isoforms (190 kDa, 270 kDa, 480 kDa) by HA-IP versus input in *NG2*^{CreERTM};RiboTag mice. Data are plotted as Mean±SEM. Each data point represents an individual animal (N = 3, except N = 2 for AnkG480 as Cq is undetectable in one IP sample). **e** Volcano plot of differentially expressed genes between AnkG icKO IP sample and control IP sample. Magenta dots represent significantly upregulated genes, blue dots represent significantly downregulated genes, and gray dots represent genes that are not statistically differentially expressed (dashed lines:

$-\log_{10}(p - value) = 2$ and $|\log_2 FC| = 1$). Differential gene expression analysis was performed using edgeR under a negative binomial generalized linear model with quasi-likelihood dispersion estimates, assuming an FDR < 0.1 as significant. Genes-of-interest are labeled individually (Blue: oligodendrocyte-specific genes. Magenta: cytoskeletal components. Black: other relevant genes-of-interest). **f** Immunoblot of AnkB and spectrins from 14 month-old cKO and control mouse brain. Experiments were performed three times. **g, h** Immunofluorescence labeling of AnkB (magenta) with βIV-spectrin (cyan) in the optic nerve of 6 month-old (**g**) and 14 month-old (**h**) control and cKO mice. Experiments were performed in replicates. Scale bar, 50 μm and 10 μm, respectively. Solid arrowheads indicate nodes of Ranvier. Empty arrowheads indicate AnkB+ paranodes. **i** Gene ontology analysis of significantly enriched differentially regulated cellular component (CC, solid bar) and molecular functions (MF, empty bar) in AnkG icKO RiboTag vs control RiboTag mice. Adjusted p-value is calculated based on clusterProfiler and pathview. Downregulated CC and MF (blue), and upregulated CC and MF (magenta). Enrichment scores are calculated by $-\log_{10}(p - value)$. Source data are provided as a Source Data file.

---

stop codon in exon 24. *Ank3*$^{F/F}$ mice (B6.129-Ank3$^{tm2.1Bnt}$/J) were generated as previously described[45] (RRID:IMSR_JAX:029797). *NG2*^{Cre} mice were obtained from The Jackson Laboratory (RRID:IMSR_JAX:008533). Only female *NG2*^{Cre} mice were used as breeders to avoid potential germ-line transmission. Both female and male mice were used for experiments. AnkG inducible conditional knockout mice (AnkG icKO) were generated using *NG2*^{CreERTM} mice (RRID:IMSR_JAX:008538). Tamoxifen (T5648-1G) solution was prepared at a concentration of 20 mg/ml in 5% ethanol and 95% corn oil and was administered intraperitoneally for 5 consecutive days (100 mg/kg of body weight) to 8 week-old mice which were analyzed after one month. RiboTag mice (B6J.129(Cg)-Rpl22tm1.1Psam/SjJ) were obtained from The Jackson Laboratory (RRID:IMSR_JAX:029977).

Genotyping for all transgenic animals was carried out by standard PCR on tail clips and further confirmed by immunofluorescence and or immunoblotting. Both specificity and efficiency of the Cre lines were assessed using an Ai3 reporter line. The following primers were used for genotyping:

Ank3$^{F/F}$ Forward: 5′ - TTA ATT TGG GGA GGG GGG AGT C - 3′
Ank3$^{F/F}$ Reverse: 5′ - TTG GGA TGC TTT GAT TCA GGG - 3′
Cre Forward: 5′ - TGC TGT TTC ACT GGT TAT GCG G - 3′
Cre Reverse: 5′ - TTG CCC CTG TTT CAC TAT CCA G - 3′
RiboTag Forward: 5′ - GGG AGG CTT GCT GGA TAT G - 3′
RiboTag Reverse: 5′ - TTT CCA GAC ACA GGC TAA GTA CAC - 3′

Behavioral analyses

Similar numbers of male and female littermate mice were used for behavioral experiments. The age and number of animals are specified for each experiment and indicated in the figure legend. Sex is specified for each data point in the Source Data File. Whenever no sex-specific differences were observed, male and female mice were pooled together based on age and genotypes for statistical analyses. To eliminate odor cues, all apparatuses were cleaned with ethanol, dried, and ventilated between individuals during testing. Mice were handled by the experimenter for 5 consecutive days (15 minutes/day) before the series of behavioral experiments. Animals were tested at the same time each day during the light cycle with the experimenter blinded to the genotypes.

Gait analysis. Gait characteristics were measured using footprint analysis[38]. In short, the hind feet of adult mice were painted with washable, nontoxic paint before walking through a 45 cm custom-made tunnel. The footprints were collected by white paper fitted to the floor and measured with ImageJ. For each animal, at least 20 representative and legible steps were analyzed, and the average value was used for quantitative analyses. Stride was measured from one left footprint to the next, sway was measured by the horizontal width

between left and right foot, and stance was measured by the diagonal distance between left and right feet.

Open field test. The open field test was used to assess general locomotion. Briefly, adult mice were placed in the center of an open Plexiglass arena (40 × 40 cm, height 40 cm) and allowed to explore freely for 10 minutes. A ceiling-mounted camera was used to video tape all experiments. Automatic tracking of the animals is performed in the AnyMaze software (Stoelting Co.). The parameters reported here include distance traveled and time spent in the inner zone throughout the 10 min test period. The inner zone was defined as the center 20 × 20 cm area.

Rotarod. The rotarod test was conducted to assess motor function and motor learning. Young adult mice (3 month-old) were acclimated to walking on the rotating rod at a constant speed of 4 rpm for 1 minute. After a 30-minute break, they were placed onto the rotarod accelerating from 4 rpm to 40 rpm for 5 minutes. Three trials were performed on each day for three consecutive days, with a 1-hour break in between two trials. The latency to fall was triggered by the lever or manually recorded—if the animal passively clutched onto the rod for two full rotations, the time was recorded as latency to fall. The average time for three trials on each day was calculated and used for quantitative and statistical analyses.

Elevated plus maze. The elevated plus maze (EPM) test was performed to assess anxiety[46]. An apparatus consisting of four metal arms is used, with two open and two enclosed arms perpendicular to each other (30 cm long × 5 cm wide) and raised 40 cm above the floor. Adult mice were placed at the intersection between open and closed arms, with their heads towards the open arm. Animals were automatically tracked by a camera and the AnyMaze system. Time spent in each of the arms was reported. If an animal fell from or jumped off the EPM apparatus, it is excluded from the analysis.

Three-chamber social test. The three-chamber test was performed to assess the sociability and social novelty of the animals (Fig. 7c)[47]. In brief, the test consisted of three 10-minute stages, including habituation, sociability, and social novelty stages. In the first 10 minutes, adult mice were allowed to freely explore a 60 × 40 × 23 cm Plexiglass arena with three equally sized, interconnected chambers (left, center, and right). The left and right chamber each contained an empty wire-cup. During the next 10 minutes, the mice were placed back in the center, with another age- and sex-matched stranger animal placed in a randomly chosen wire-cup. In the last 10 minutes, a second stranger mouse was introduced into the remaining empty cup. Time spent interacting with each cup or mouse was recorded using a camera and

the automated AnyMaze software and manually scored to include only the active interactions (sniffing, crawling upon, etc.). Sociability was evaluated by preference to animal versus empty cup, and social novelty was examined by preference to stranger versus familiar mouse.

Fear conditioning test. The fear conditioning test was performed to assess the learning and memory function[48]. Briefly, adult mice were habituated to the conditioning chamber 20 minutes per day for 3 consecutive days (Fig. 7g). On the training day, mice received a foot shock (0.35 mA, 1 s) after 2 minutes in the conditioning chamber and remained in the chamber for another 2 minutes before returning to their home cage. 24 hours after training, mice were returned to the conditioning chamber for 5 minutes without any foot shock and the percentage of time spent freezing was recorded and analyzed by the FreezeFrame and FreezeView software.

Tail suspension test. The tail suspension test was performed to assess learnt helplessness behaviors in adult mice[49]. To prevent tail-climbing behaviors, the tail of a subject mouse was first passed through a small plastic cylinder prior to suspension. The end of the tail was adhered to an adhesive tape that sticks back onto itself, with 2-3 mm of tail remaining outside of the tape. The free end of the tape was then applied to a horizontal suspension bar so that the approximate distance between the mouse's nose and the apparatus floor was 20 to 25 cm. Each test lasted 6 minutes. A camera and the AnyMaze software were used to record and score the immobility of each animal.

Electrophysiology
Compound action potential (CAP) recording was performed to assess the signal transduction velocity in optic nerves[15]. Briefly, optic nerves were dissected out and submerged in oxygenated Locke's solution bath at 25 °C (154 mM NaCl, 2 mM CaCl$_2$, 5.6 mM KCl, 10 mM HEPES, pH adjusted to 7.4 with NaOH) supplemented with 1 mg/ml glucose. The non-myelinated transparent portion at the anterior end of the optic nerve was trimmed off. The remaining myelinated optic nerve was sealed into suction electrodes, with the anterior in the stimulating electrode and the posterior in the recording electrode. Increasing currents were applied using MultiClamp 700B until a supra-maximal threshold was reached, at which the CAP was subsequently recorded. Data were visualized and analyzed in Clampex 10.7 and Clampfit 10.7. The conduction velocity was calculated by dividing the length of the recorded optic nerve by the latency (from stimulus onset to maximal peak). The recording traces of CAP were fitted into three Gaussian curves using python, to further assess the heterogeneous groups of axons with fast, medium, and slow conducting velocities. The experimenter was blinded to the genotype of the animals as they were identified only by the ear-tag numbers without the genotyping information.

Immunofluorescence staining
Mice were anesthetized with isoflurane, followed by transcardial perfusion with ice-cold PBS and then 4% paraformaldehyde (PFA). Tissues of interest were dissected out and post-fixed in 4% PFA at 4 °C. All tissues were identified by the ear-tag number of the animals so that the experimenter is blinded to the genotypes. Optic nerves were post-fixed for 30 minutes, transferred to 20% sucrose in 0.1 M phosphate buffer (PB) overnight, embedded in Tissue-Tek OCT (Sakura Finetek 4583) and sectioned using Microtome HS 450 at an interval of 10 μm. Knockout and littermate control tissues were mounted onto the same 1% bovine gelatin-coated glass coverslips, air-dried at room temperature (RT) before staining. Brains and spinal cords were post-fixed at 4 °C overnight, dehydrated in 20% sucrose in 0.1 M PB and 30% sucrose in 0.1 M PB at 4 °C overnight. Tissues were embedded in OCT compound and stored at -80 °C before sectioning. Cryostat sections were

made at 20 μm intervals and mounted onto Superfrost Plus slides (Fisher Scientific Cat# 1255015), with knockout and littermate control tissues on the same slide for comparison.

Coverslips or Superfrost Plus slides with tissues were first washed three times, 5 minutes each, with 0.1 M PB to remove residue OCT. They were then blocked with phosphate buffer with detergent and goat serum (PBTGS: 0.1 M PB, 10% normal goat serum, 0.3 - 0.5% Triton X-100) for 1 hour at RT. Primary antibodies diluted in PBTGS were added and incubated in a humid chamber at 4 °C overnight. After washing three times with PBTGS, 5 minutes each, secondary antibodies diluted in PBTGS were added and incubated at RT for 1 hour. Samples were then washed with PBTGS, 0.1 M PB, and 0.05 M PB three times each before mounted with VECTASHIELD HardSet Antifade Mounting Medium (Vector Laboratories Cat# H-1400-10) and imaged with a Zeiss Apotome.2 Microscope.

Protein extraction and immunoblotting
Animals were euthanized with isoflurane and immediately perfused transcardially with ice-cold PBS. Brains and spinal cords were quickly dissected out, snap-frozen in liquid nitrogen and stored at -80 °C. Frozen tissues were homogenized in glass Dounce Homogenizer on ice with fresh homogenization buffer: 50 mM Tris-HCl, 15 mM EGTA, 100 mM NaCl, and 1 mM DTT, supplemented with cOmplete protease inhibitor cocktail (Roche Cat# 11836170001) and PMSF immediately before use. Crude homogenates were first centrifuged using the Eppendorf 5417 R Refrigerated Centrifuge at 2000 rpm (425Xg) at 4 °C for 10 minutes to remove cell debris. The supernatant was then centrifuged at 13,000 rpm (17949Xg) at 4 °C for another 90 minutes. Soluble proteins were present in the supernatant, and membrane-bound proteins were retrieved from the precipitated fraction and resuspended in the homogenization buffer. The concentration of each protein sample was measured using BCA assay (Pierce Cat# A55864) and adjusted before boiling in SDS reducing sample buffer at 95 °C for 10 minutes and centrifuged at 5000 rpm (2655Xg) for 5 minutes.

20 μg of total protein was resolved on 6% or 14% polyacrylamide gels using electrophoresis (SDS-PAGE) depending on the molecular weight of the target protein and transferred onto 0.45 μm nitrocellulose membrane using Bio-Rad Trans-blot system. Ponceau S was briefly added to the membrane to evaluate the quality of transfer and washed away using TBST (TBS with 0.1% Tween-20). The membrane was blocked with Blotto solution (5% skim milk in TBST) for 1 hr at RT. Primary antibodies against proteins of interest were diluted in Blotto solution and incubated with the membrane at 4 °C overnight. The membrane was then washed with TBST for three times, 10 minutes each, and then incubated with HRP-conjugated secondary antibodies in Blotto solution for 1 hour at RT. The membrane was then washed with TBST three times before developing signals using SuperSignal West Pico PLUS (Pierce Cat# 34580) and imaging with the LI-COR Odyssey Fc system. The membrane was then washed with TBS for three times at RT, stripped with Restore PLUS Western Blot Stripping Buffer (Thermo Scientific Cat# 46430) for 15 minutes at RT, re-blocked with Blotto solution for 30 minutes at RT, and re-incubated with primary antibodies against housekeeping genes, such as β-Actin and α-Tubulin for 3 hours at RT. Subsequent washing, secondary incubation and signal detection were performed as described above. Densitometry measurements of immunoblots were performed in FIJI/ImageJ (RRID:SCR_003070).

Antibodies
For standard immunofluorescence staining, the following primary antibodies were used: Mouse monoclonal antibodies against AnkG (UC Davis/NIH NeuroMab Facility Cat# N106/65, RRID:AB_2877525, 1:500), Caspr (UC Davis/NIH NeuroMab Facility Cat# K65/35, RRID:AB_2877274, 1:1000), Kv1.2 (UC Davis/NIH NeuroMab Facility Cat#

K14/16, RRID:AB_2877295, 1:1000), APC/CC-1 (Millipore Cat# OP80, RRID:AB_2057371, 1:1000), HA.11 Epitope Tag (BioLegend Cat# 901505, RRID:AB_2565023, 1:1000) and Calbindin (UC Davis/NIH NeuroMab Facility Cat# L109/57, RRID:AB_2877197, 1:1000). A rabbit monoclonal antibody against Neurofascin 186 (Cell Signaling Technology Cat# 15034, RRID:AB_2773024, 1:500). Rabbit polyclonal antibodies against Caspr (Abcam Cat# ab34151, RRID:AB_869934, 1:1000), MBP (Abcam Cat# ab40390, RRID:AB_1141521, 1:500), and βIV-spectrin (M.N. Rasband, Baylor College of Medicine, Texas, USA Cat# bIV SD, RRID:AB_2315634, 1:500). A chicken polyclonal antibody against GFAP (Abcam Cat# ab134436, RRID:AB_2818977, 1:2000). A guinea pig polyclonal antibody against AnkG (Synaptic Systems Cat# 386 004, RRID:AB_2725774, 1:500). All Alexa Fluor-conjugated secondary antibodies were purchased from Thermo Fisher Scientific and used with dilution 1:500. Isotype specific secondary antibodies were used for monoclonal primary antibodies whenever possible.

For immunoblotting, the following primary antibodies were used: Mouse monoclonal antibodies against Contactin (UC Davis/NIH NeuroMab Facility Cat# K73/20, RRID:AB_2877311, 1:2000), MBP (BioLegend Cat# 836504, RRID:AB_2616694, 1:2000), αII Spectrin (BioLegend Cat# 803201, RRID:AB_2564660, 1:2000), βII Spectrin (BD Biosciences Cat# 612563, RRID:AB_399854, 1:2000), α-Tubulin (Sigma-Aldrich Cat# T6074, RRID:AB_477582, 1:5000), β-Actin (Sigma-Aldrich Cat# A1978, RRID:AB_476692, 1:5000), and β-Actin-HRP (C4) (Santa Cruz Biotechnology Cat# sc-47778, RRID:AB_626632, 1:1000). Rabbit polyclonal antibodies against Caspr (Abcam Cat# ab34151, RRID:AB_869934, 1:3000), Calbindin D-28K (Millipore Cat# AB1778, RRID:AB_2068336, 1:2000), MBP (Abcam Cat# ab40390, RRID:AB_1141521, 1:2000), AnkB (M.N. Rasband, Baylor College of Medicine, Texas, USA Cat# anti-AnkB, RRID:AB_2315635, 1:1000), and βIII Spectrin (Novus Cat# NB110-58346, RRID:AB_877723). Chicken polyclonal antibodies against GFAP (Abcam Cat# ab134436, RRID:AB_2818977, 1:4000) and Neurofascin (R&D Systems Cat# AF3235, RRID:AB_10890736, 1:2000). A guinea pig polyclonal antibody against AnkG (Synaptic Systems Cat# 386 004, RRID:AB_2725774, 1:2000). All HRP-conjugated secondary antibodies were purchased from Jackson ImmunoResearch Laboratories and used with dilution 1:5000.

For immunoprecipitation, a primary antibody against HA.11 (BioLegend Cat# 901505; RRID:AB_2565023, 1:200) was used.

Transmission electron microscopy

Transmission electron microscopy was used to assess the ultra-structure of the myelin sheaths. Mice were anesthetized and perfused with a fixative containing 4% PFA and 2.5% glutaraldehyde in 0.1 M cacodylate buffer (pH 7.4). Dorsal roots with DRG were then isolated and incubated overnight in the same fixative at RT and stored at 4 °C. After washing with 0.1 M cacodylate buffer, the samples were post-fixed with 1% osmium tetroxide, 0.5% potassium dichromate, and 0.5% potassium hexacyanoferrate in cacodylate buffer and stained with 2% aqueous uranyl acetate followed by ethanol dehydration. The samples were then embedded in Epoxy resin (Agar Scientific), and sections of 70 nm were cut and stained with Reynolds' lead citrate. Samples were examined using a FEI Tecnai T12 transmission electron microscope equipped with an XF416 TVIP camera.

Image processing

Immunofluorescence images were observed with an AxioImager (Carl Zeiss) with the Apotome optical sectioning module and acquired with a digital camera (AxioCam, Carl Zeiss). Images from the same experiments were acquired and processed in batch using the ZEN software (Carl Zeiss) under identical parameters. All images were identified by the ear-tag number of the animals so that the experimenter is blinded to the genotypes. For z-stack images, maximum intensity projection (MIP) function was applied. For better visualization of representative PNJs, images were taken at the magnification of 100x and cropped in Adobe Photoshop software, with each channel isolated and inverted. Relative intensity measurements of fluorescence images and densito-metry analysis of immunoblots were performed in FIJI/ImageJ (RRID:SCR_003070). Nearest neighbor analysis was performed using the ND plugin in FIJI/ImageJ. The density of Purkinje cells was calculated by the number of Calbindin⁺ cells divided by the length of the Purkinje layer. The relative fold-changes were calculated by normalizing knockout to littermate controls. At least 3 images from 3 different animals per genotype were included for each analysis.

For TEM images, axons, inner boundary, and outer boundary of myelin sheaths were identified semi-automatically by MyelTracer and corrected manually whenever necessary. G-ratios were automatically calculated in MyelTracer[50].

Statistical analyses

Statistical analyses for immunofluorescence images, immunoblots, and behavioral assays were performed in GraphPad Prism10 (RRID:SCR_002798). No power analyses were performed to pre-determine the sample sizes, but our sample sizes are comparable to those previously reported[15]. For histological analyses, at least three age- and sex-matched littermates were selected per genotype. If there were fewer than three pairs, mice from another litter with similar birth date were added for statistical analyses. For electrophysiological analyses, traces from 7 control optic nerves and 8 AnkG cKO optic nerves were analyzed.

Data were analyzed using Microsoft Excel, python, and GraphPad Prism 10. All statistical analyses were performed in Prism. The raw data were first examined to identify and exclude outliers. The cleaned data were then tested for normality and variance within each group, based on which the proper tests were selected with consideration of repeated measurements or multiple comparisons. All tests are two-tailed unless otherwise stated. The following tests were employed where appropriate: unpaired Student's t-test, Welch's t-test, Mann-Whitney U test, one-way ANOVA, two-way ANOVA with multiple comparisons, Chi-square test, and Kolmogorov–Smirnov test. Each individual data point is plotted within each graph. All bar plots represent mean ± SEM unless otherwise indicated.

RNA purification and sequencing

Actively translated mRNAs from the oligodendrocyte lineage were isolated and prepared as previously described[51]. Briefly, *NG2^CreERTM*; RiboTag mice were injected with tamoxifen (20 mg/ml in 5% ethanol and 95% corn oil) for 5 consecutive days (100 mg/kg of body weight) at 2 months of age and harvested 1 month later. Mice were anesthetized with isoflurane and perfused with ice-cold PBS, and the whole brain homogenates were immediately processed for IP-enrichment of ribosomes from oligodendrocytes. Three animals were pooled together for one RNA-seq sample. 10% of the cleared homogenate was collected as input. IP was performed overnight with HA-antibody (Biolegend Cat# 901505; RRID:AB_2565023) and Pierce protein A/G Magnetic Beads (Thermo Fisher Scientific Cat# 88803). RNA was isolated from both input and IP samples using RNeasy Mini Kit (Qiagen Cat# 74104).

NanoDrop spectrophotometry (Thermo Fisher Scientific) was used to assess RNA purity while RNA integrity was evaluated using a 2100 Bioanalyzer with RNA chips (Agilent Technologies, Santa Clara, CA). The Genomic and RNA Profiling Core prepared libraries with the Takara SMARTer® Stranded Total RNA-Seq v3 - Pico Input Mammalian kit (Takara, p/n 634485). Using the KAPA Library Quantification kit for Illumina platforms (KAPA Biosystems, Wilmington, MA), libraries were quantitated and pooled equimolarly. Sequencing of mRNA libraries was performed on an Illumina NovaSeq 6000 platform to around 90 million read pairs per sample.

cDNA synthesis and quantitative PCR

cDNA was synthesized from both IP and input RNA samples as previously described[52]. Briefly, IP and input RNA samples were reverse transcribed into cDNA using SuperScript IV VILO MasterMix, followed by genomic DNA removal with ezDNase Enzyme (Invitrogen Cat# 11766050). And quantitative PCR (qPCR) was performed using iTaq Universal SYBR Green Supermix (Bio-Rad Cat# 1725122) using the StepOnePlus Real-Time PCR System. Melting curve plots were examined to ensure specificity. The relative expression of genes-of-interest was quantified using the $2^{-\Delta\Delta CT}$ method, with *RplpO* serving as the internal control.

The following primers were used for the qPCR:

Olig2 Forward: 5' - GAA CCC CGA AAG GTG TGG AT - 3'
Olig2 Reverse: 5' - GCC CCA GGG ATG ATC TAA GC - 3'
Aldh1l1 Forward: 5' - ATG ATC ATC TCT CGG TTT GCT GA - 3'
Aldh1l1 Reverse: 5' - CAT CGG TCT TGT TGT ATG TGT TG - 3'
Rbfox3 (NeuN) Forward: 5' - GCG GTC GTG TAT CAG GAT GG - 3'
Rbfox3 (NeuN) Reverse: 5' - CGA TGC TGT AGG TTG CTG TG - 3'
AnkG-190 Forward: 5' - CTT TGC CTC CCT AGC TTT AC - 3'
AnkG-190 Reverse: 5' - TCT GTC CAA CTA AGT CCC AG - 3'
AnkG-270 Forward: 5' - GCC ATG TCT CCA GAT GTT G - 3'
AnkG-270 Reverse: 5' - TCT GTC CAA CTA AGT CCC AG - 3'
AnkG-480 Forward: 5' - GAG GCA CCG CCC TTA AA - 3'
AnkG-480 Reverse: 5' - GCC AGC TCT GTC CAA CTA A - 3'
RplpO Forward: 5' - CAG GCG TCC TCG TTG GAG - 3'
RplpO Reverse: 5' - ATC TGC TGC ATC TGC TTG GAG - 3'

Bioinformatics analyses

The first 14 nucleotides from Read 2 FastQ files were trimmed to remove UMI, UMI linker, and Pico v3 SMART UMI Adapter sequences. Illumina adapters were trimmed from raw reads using Cutadapt v4.4[53], removing the following adapter sequences: Read1: AGATCGGAAGAGCACACGTCTGAACTCCAGTCA, Read2: AGATCGGAAGAGCGTCGTGTAGGGAAAGAGTGT. Quality trimming and filtering was performed using Trimmomatic v0.39[54] to trim the first 5 base calls, to trim read segments that fall below a quality score of 25 using SLIDINGWINDOW:4:25, and retain reads with a minimum length of 100 bp. Reads were then aligned to UCSC mm10 using STAR v2.7.10b[55] with gene quantification generated using (quantMode GeneCounts).

Raw counts were filtered based on CPM, retaining genes with CPM > 1.5 for at least 2 samples. Visualization and downstream analyses were performed using R. Normalization was performed with the R program edgeR[56], TMM normalization. Differential gene expression analysis was also performed using edgeR under a negative binomial generalized linear model with quasi-likelihood dispersion estimates, assuming an FDR < 0.1 as significant.

The volcano plot of differentially expressed genes was generated by GraphPad Prism10. Bar plot of Gene Ontology and KEGG pathway enrichment analyses was generated using SRplot[57], which is based on clusterProfiler[58] and pathview[59].

Reporting summary

Further information on research design is available in the Nature Portfolio Reporting Summary linked to this article.

Data availability

All data generated or analyzed during this study are included in this published paper. The RNA-seq data generated in this study have been deposited in the Gene Expression Omnibus (GEO) database under accession code GSE263546. Source data are provided with this paper.

References

1. Hedstrom, K. L., Ogawa, Y. & Rasband, M. N. AnkyrinG is required for maintenance of the axon initial segment and neuronal polarity. *J. Cell Biol.* **183**, 635–640 (2008).
2. Zhou, D. et al. AnkyrinG is required for clustering of voltage-gated Na channels at axon initial segments and for normal action potential firing. *J. Cell Biol.* **143**, 1295–1304 (1998).
3. Stevens, S. R. & Rasband, M. N. Pleiotropic ankyrins: scaffolds for ion channels and transporters. *Channels (Austin)* **16**, 216–229 (2022).
4. Jenkins, P. M. et al. Giant ankyrin-G: a critical innovation in vertebrate evolution of fast and integrated neuronal signaling. *Proc. Natl Acad. Sci. USA* **112**, 957–964 (2015).
5. Rasband, M. N. & Peles, E. Mechanisms of node of Ranvier assembly. *Nat. Rev. Neurosci.* **22**, 7–20 (2021).
6. Bhat, M. A. et al. Axon-glia interactions and the domain organization of myelinated axons requires neurexin IV/Caspr/Paranodin. *Neuron* **30**, 369–383 (2001).
7. Rios, J. C. et al. Paranodal interactions regulate expression of sodium channel subtypes and provide a diffusion barrier for the node of Ranvier. *J. Neurosci.* **23**, 7001–7011 (2003).
8. Amor, V. *et al.* The paranodal cytoskeleton clusters Na(+) channels at nodes of Ranvier. *eLife* **6** https://doi.org/10.7554/eLife.21392 (2017).
9. Dupree, J. L., Girault, J.-A. & Popko, B. Axo-glial interactions regulate the localization of axonal paranodal proteins. *J. Cell Biol.* **147**, 1145–1151 (1999).
10. Tait, S. et al. An oligodendrocyte cell adhesion molecule at the site of assembly of the paranodal axo-glial junction. *J. Cell Biol.* **150**, 657–666 (2000).
11. Menegoz, M. et al. Paranodin, a glycoprotein of neuronal paranodal membranes. *Neuron* **19**, 319–331 (1997).
12. Boyle, M. E. et al. Contactin orchestrates assembly of the septate-like junctions at the paranode in myelinated peripheral nerve. *Neuron* **30**, 385–397 (2001).
13. Zhang, C., Susuki, K., Zollinger, D. R., Dupree, J. L. & Rasband, M. N. Membrane domain organization of myelinated axons requires betaII spectrin. *J. Cell Biol.* **203**, 437–443 (2013).
14. Horresh, I., Bar, V., Kissil, J. L. & Peles, E. Organization of myelinated axons by Caspr and Caspr2 requires the cytoskeletal adapter protein 4.1B. *J. Neurosci.* **30**, 2480–2489 (2010).
15. Chang, K. J. et al. Glial ankyrins facilitate paranodal axoglial junction assembly. *Nat. Neurosci.* **17**, 1673–1681 (2014).
16. Ferreira, M. A. et al. Collaborative genome-wide association analysis supports a role for ANK3 and CACNA1C in bipolar disorder. *Nat. Genet* **40**, 1056–1058 (2008).
17. Schizophrenia Psychiatric Genome-Wide Association Study, C. Genome-wide association study identifies five new schizophrenia loci. *Nat. Genet* **43**, 969–976 (2011).
18. Codina-Sola, M. et al. Integrated analysis of whole-exome sequencing and transcriptome profiling in males with autism spectrum disorders. *Mol. autism* **6**, 21 (2015).
19. Iqbal, Z. et al. Homozygous and heterozygous disruptions of ANK3: at the crossroads of neurodevelopmental and psychiatric disorders. *Hum. Mol. Genet.* **22**, 1960–1970 (2013).
20. Leussis, M. P. et al. The ANK3 bipolar disorder gene regulates psychiatric-related behaviors that are modulated by lithium and stress. *Biol. psychiatry* **73**, 683–690 (2013).
21. Zhu, S. et al. Genetic disruption of ankyrin-G in adult mouse forebrain causes cortical synapse alteration and behavior reminiscent of bipolar disorder. *Proc. Natl Acad. Sci. USA* **114**, 10479–10484 (2017).
22. Lopez, A. Y. et al. Ankyrin-G isoform imbalance and interneuronopathy link epilepsy and bipolar disorder. *Mol. psychiatry* **22**, 1464–1472 (2017).
23. Zhang, Y. et al. An RNA-sequencing transcriptome and splicing database of glia, neurons, and vascular cells of the cerebral cortex. *J. Neurosci.* **34**, 11929–11947 (2014).

24. Susuki, K. et al. Glial betaII spectrin contributes to paranode formation and maintenance. *J. Neurosci.* **38**, 6063–6075 (2018).

25. Susuki, K. et al. Three mechanisms assemble central nervous system nodes of Ranvier. *Neuron* **78**, 469–482 (2013).

26. Foster, R. E., Connors, B. W. & Waxman, S. G. Rat optic nerve: electrophysiological, pharmacological and anatomical studies during development. *Brain Res.* **255**, 371–386 (1982).

27. Pillai, A. M. et al. Spatiotemporal ablation of myelinating glia-specific neurofascin (Nfasc NF155) in mice reveals gradual loss of paranodal axoglial junctions and concomitant disorganization of axonal domains. *J. Neurosci. Res* **87**, 1773–1793 (2009).

28. Garcia-Fresco, G. P. et al. Disruption of axo-glial junctions causes cytoskeletal disorganization and degeneration of Purkinje neuron axons. *Proc. Natl Acad. Sci. USA* **103**, 5137–5142 (2006).

29. Davis, K. L. et al. White matter changes in schizophrenia: evidence for myelin-related dysfunction. *Arch. Gen. Psychiatry* **60**, 443–456 (2003).

30. Lewandowski, K. E. et al. Myelin vs axon abnormalities in white matter in bipolar disorder. *Neuropsychopharmacology* **40**, 1243–1249 (2015).

31. Leussis, M. P., Madison, J. M. & Petryshen, T. L. Ankyrin 3: genetic association with bipolar disorder and relevance to disease pathophysiology. *Biol. mood anxiety Disord.* **2**, 18 (2012).

32. Nelson, A. D. & Jenkins, P. M. Axonal membranes and their domains: assembly and function of the axon initial segment and node of ranvier. *Front. Cell. Neurosci.* **11**, 136 (2017).

33. Shepherd, M. N., Pomicter, A. D., Velazco, C. S., Henderson, S. C. & Dupree, J. L. Paranodal reorganization results in the depletion of transverse bands in the aged central nervous system. *Neurobiol. Aging* **33**, 203 e213–203.e224 (2012).

34. Takagishi, Y., Katanosaka, K., Mizoguchi, H. & Murata, Y. Disrupted axon-glia interactions at the paranode in myelinated nerves cause axonal degeneration and neuronal cell death in the aged Caspr mutant mouse shambling. *Neurobiol. Aging* **43**, 34–46 (2016).

35. Nawaz, S. et al. Actin filament turnover drives leading edge growth during myelin sheath formation in the central nervous system. *Dev. Cell* **34**, 139–151 (2015).

36. Jung, J. et al. Actin polymerization is essential for myelin sheath fragmentation during Wallerian degeneration. *J. Neurosci.* **31**, 2009–2015 (2011).

37. Luft, A. R. et al. Patterns of age-related shrinkage in cerebellum and brainstem observed in vivo using three-dimensional MRI volumetry. *Cereb. Cortex* **9**, 712–721 (1999).

38. Stevens, S. R. et al. Ankyrin-R Links Kv3.3 to the spectrin cytoskeleton and is required for purkinje neuron survival. *J. Neurosci.* **42**, 2–15 (2022).

39. Andersen, B. B., Gundersen, H. J. & Pakkenberg, B. Aging of the human cerebellum: a stereological study. *J. Comp. Neurol.* **466**, 356–365 (2003).

40. Chao, O. Y. et al. Social memory deficit caused by dysregulation of the cerebellar vermis. *Nat. Commun.* **14**, 6007 (2023).

41. Chao, O. Y., Zhang, H., Pathak, S. S., Huston, J. P. & Yang, Y. M. Functional convergence of motor and social processes in lobule IV/V of the mouse cerebellum. *Cerebellum* **20**, 836–852 (2021).

42. Bozdagi, O. et al. Haploinsufficiency of the autism-associated Shank3 gene leads to deficits in synaptic function, social interaction, and social communication. *Mol. autism* **1**, 15 (2010).

43. Gupta, M. et al. TSPAN5, ERICH3 and selective serotonin reuptake inhibitors in major depressive disorder: pharmacometabolomics-informed pharmacogenomics. *Mol. psychiatry* **21**, 1717–1725 (2016).

44. Hughes, T. et al. A loss-of-function variant in a minor isoform of ANK3 protects against bipolar disorder and schizophrenia. *Biol. psychiatry* **80**, 323–330 (2016).

45. Jenkins, P. M. et al. E-cadherin polarity is determined by a multi-function motif mediating lateral membrane retention through ankyrin-G and apical-lateral transcytosis through clathrin. *J. Biol. Chem.* **288**, 14018–14031 (2013).

46. Stevens, S. R. et al. Ankyrin-R regulates fast-spiking interneuron excitability through perineuronal nets and Kv3.1b K(+) channels. *eLife* **10** https://doi.org/10.7554/eLife.66491 (2021).

47. Buffington, S. A. et al. Microbial Reconstitution Reverses Maternal Diet-Induced Social and Synaptic Deficits in Offspring. *Cell* **165**, 1762–1775 (2016).

48. Stoica, L. et al. Selective pharmacogenetic inhibition of mammalian target of Rapamycin complex I (mTORC1) blocks long-term synaptic plasticity and memory storage. *Proc. Natl Acad. Sci. USA* **108**, 3791–3796 (2011).

49. Can, A. et al. The tail suspension test. *J Vis Exp*, e3769 (2012).

50. Kaiser, T. et al. MyelTracer: A Semi-Automated Software for Myelin g-Ratio Quantification. *eNeuro* **8** https://doi.org/10.1523/ENEURO.0558-20.2021 (2021).

51. Bravo-Ferrer, I., Khakh, B. S. & Diaz-Castro, B. Cell-specific RNA purification to study translatomes of mouse central nervous system. *STAR Protoc.* **3**, 101397 (2022).

52. Sert, O. et al. Postsynaptic beta1 spectrin maintains Na(+) channels at the neuromuscular junction. *J. Physiol.* https://doi.org/10.1113/JP285894 (2024).

53. Martin, M. Cutadapt Removes Adapter Sequences From High-Throughput Sequencing Reads. *EMBnet. J.* **17**, 10–12 (2011).

54. Bolger, A. M., Lohse, M. & Usadel, B. Trimmomatic: a flexible trimmer for Illumina sequence data. *Bioinformatics* **30**, 2114–2120 (2014).

55. Dobin, A. et al. STAR: ultrafast universal RNA-seq aligner. *Bioinformatics* **29**, 15–21 (2013).

56. Robinson, M. D., McCarthy, D. J. & Smyth, G. K. edgeR: a Bioconductor package for differential expression analysis of digital gene expression data. *Bioinformatics* **26**, 139–140 (2010).

57. Tang, D. et al. SRplot: A free online platform for data visualization and graphing. *PLoS One* **18**, e0294236 (2023).

58. Yu, G., Wang, L. G., Han, Y. & He, Q. Y. clusterProfiler: an R package for comparing biological themes among gene clusters. *OMICS* **16**, 284–287 (2012).

59. Luo, W. & Brouwer, C. Pathview: an R/Bioconductor package for pathway-based data integration and visualization. *Bioinformatics* **29**, 1830–1831 (2013).

Acknowledgements

Author contributions

Conceptualization, methodology, data curation, validation, investigation, visualization, and writing—original draft and editing: X.D.; Investigation and data curation: Y.W., A.V., V.R., E.R.; Investigation and resources: J.T.O. Resources and validation: Y.L.; Data curation, analysis, resources, and writing—editing: D.C.K. and E.P.; Conceptualization, methodology, data curation, writing—editing, project administration, and funding acquisition: M.N.R.

Competing interests

The authors declare no competing interests.

Additional information

Supplementary information The online version contains supplementary material available at
https://doi.org/10.1038/s41467-024-55209-7.

Correspondence and requests for materials should be addressed to Matthew N. Rasband.

Peer review information *Nature Communications* thanks the anonymous reviewers for their contribution to the peer review of this work. A peer review file is available.

Reprints and permissions information is available at
http://www.nature.com/reprints

Publisher's note Springer Nature remains neutral with regard to jurisdictional claims in published maps and institutional affiliations.